

# Development and application of the Ascent-Drift-Descent Radiosonde System (ADDRS)

Xiaozhong Cao\*<sup>1</sup>, Qiyun Guo<sup>2,3,4</sup>, Haowen Luo<sup>2,3,4</sup>, [Jincheng Wang<sup>5</sup>](#), Rongkang Yang<sup>2,3,4</sup>,  
[Die Xiao<sup>6</sup>](#), [Yinfeng Liu<sup>7</sup>](#), [Zhongliang Sun<sup>8</sup>](#), [Shijun Liu<sup>9</sup>](#), [Sijie Chen<sup>10</sup>](#), Anfan Huang<sup>2,3,4</sup>,  
[Guo Jianping<sup>11</sup>](#), Peng Zhang\*<sup>2,3,4</sup>

<sup>1</sup> China Meteorological Administration, Beijing, China;

<sup>2</sup> Meteorological Observation Centre of China Meteorological Administration, Beijing, China;

<sup>3</sup> State Key Laboratory of Environment Characteristics and Effects for Near-space, Beijing, China;

<sup>4</sup> Engineering Technology Research Center for Meteorological Observation of CMA, Beijing, China;

[<sup>5</sup> CMA Earth System Modeling and Prediction Centre \(CEMC\), Beijing, China;](#)

[<sup>6</sup> Hunan Key Laboratory of Near-space Meteo-ballon Materials and Technology, Zhuzhou Research & Design Institute Co, Ltd, Zhuzhou, China;](#)

[<sup>7</sup> Beijing Huayun Orient Detection Technology Co, Ltd., Beijing, China;](#)

[<sup>8</sup> Allystar Technology \(Shenzhen\) Co.LTD. , Shenzhen, China;](#)

[<sup>9</sup> Department of Advanced Technology Training of China Meteorological Administration, Beijing, China;](#)

[<sup>10</sup> National Satellite Meteorological Centre of China Meteorological Administration, Beijing, China;](#)

[<sup>11</sup> Chinese Academy of Meteorological Sciences, Beijing, China;](#)

*Corresponding author: Xiaozhong Cao, caoxzh@cma.gov.cn, Peng zhang, zhangp@cma.gov.cn.*

**ABSTRACT.** Balloon-borne radiosonde observations constitute a crucial component of meteorological sounding, which conducts a ground to upper-air “ascent phase” sounding. This paper introduces the Ascent-Drift-Descent Radiosonde System (ADDRS), an innovative system characterized by three observation phases—'Ascent-Drift-Descent' (ADD)—in which all three phases of sounding observation are executed through single balloon launch. Several key technologies were successfully developed, including the carrier (dual-mode balloon), the payload (System-on-Chip (SoC) module for radiosonde), Ground to upper-air data reception and control command transmission and data processing framework based on 'Internet cloud + Instrument terminal' was established. Data quality control methods and data assimilation techniques of ADDR S were also developed. An interactive experiment encompassing observations and forecasting was conducted to evaluate the quality of experimental data at each phase of ADDR S. Numerical assimilation and forecasting experiments showed a positive (albeit not yet statistically significant) impact on forecast quality for both general cases and for Tropical cyclone cases. The pre-operational launching and assimilation of more than 100 such radiosondes started on 1 July 2024 and provided data over one year, and the number of stations continues to grow.

## 1. Introduction

The upper-air meteorological sounding system (hereinafter referred to as 'sounding') constitutes a key element within comprehensive meteorological measurement framework (Ingleby et al., 2016a). It is responsible for gathering data on various meteorological elements such as temperature, humidity, pressure, wind speed, and wind direction from the surface up to heights of 30 km and beyond upper atmosphere (DuBois et al., 2002). This

删除[CMA MOC luo]: Guo Jianping<sup>5</sup>, Jincheng Wang<sup>6</sup>,

删除[CMA MOC luo]: <sup>7</sup>

删除[CMA MOC luo]: <sup>8</sup>

删除[CMA MOC luo]: <sup>9</sup>

删除[CMA MOC luo]: <sup>10</sup>

删除[CMA MOC luo]: <sup>1</sup>

删除[CMA MOC luo]: <sup>5</sup> Chinese Academy of Meteorological Sciences, Beijing, China;

<sup>6</sup> CMA Earth System Modeling and Prediction Centre (CEMC), Beijing, China;

<sup>7</sup>

删除[CMA MOC luo]: <sup>8</sup>

删除[CMA MOC luo]: <sup>9</sup>

删除[CMA MOC luo]: <sup>10</sup>

删除[CMA MOC luo]: <sup>1</sup>

设置格式[CMA MOC luo]: 上标

设置格式[CMA MOC luo]: 字体颜色: 自动设置

37 system provides vertically observed meteorological data for weather forecasting, numerical weather prediction,  
38 climate projection, scientific research, and the inspection and calibration of ground-based remote sensing  
39 equipment (Seidel et al., 2009; Fujiwara et al., 2025). The integration of radiosonde technology with balloon-  
40 borne soundings emerged in the 1930s, with early operational systems deployed in the 1940s; this technology  
41 has since served as a primary tool for direct measurements of upper-air meteorological elements below 30 km  
42 and is widely utilized on a global scale (Pettifer 2009; Gallice et al., 2011).

43 For nearly a century, these radiosondes have utilized the direct measurement method of “one balloon  
44 launched, one profile”. The radiosonde ascends at a certain speed with the balloon expanding in volume due to  
45 decreasing air pressure as altitude increases. Upon reaching a specific altitude, the balloon bursts, concluding  
46 the measurement process. This methodology confines effective observations to the radiosonde's ascent phase  
47 (Haig et al., 1958). The disposable nature of radiosondes and balloons necessitates significant costs for multiple  
48 deployments. Consequently, economic constraints have led to reductions in sounding operations, such as  
49 Russia's temporary reduction of launches from twice to once daily in 2015, impacting the forecasting accuracy  
50 of numerical prediction models across Northern Hemisphere countries (Ingleby et al., 2016b).

51 In recent decades, satellite soundings have played an increasing role in Numerical Weather Prediction  
52 (NWP) and are now the observations contributing most to forecast skill (Bauer et al., 2015; Bormann et al.,  
53 2019; WMO, 2024). While radio occultation data has gained importance as a reference standard (Bauer et al.,  
54 2014), radiosonde profiles still provide an important contribution to forecast skill, help with the calibration and  
55 validation of satellite soundings and allow independent verification of forecast fields. But the temporal  
56 resolution of global radiosonde observations data remains limited, posing a significant challenge to its capacity  
57 in fulfilling the requirements of routine forecasting. A notable concern arises from the scarcity of direct  
58 measurement data during periods characterized by frequent severe convective activity, particularly in the hours  
59 immediately following noon. Several studies have demonstrated that the frequent acquisition of descent  
60 radiosonde data can enhance the accuracy of numerical weather forecasting. Some multi-year studies (Cohn et  
61 al., 2013; Wang et al., 2015) suggest that assimilation of dropsonde data can reduce hurricane trajectory short-  
62 range forecast errors by 10-15%. However other studies reviewed by Majumdar (2016) show less impact.

63 Additionally, several institutions are actively investigating techniques to obtain multiple radiosonde data  
64 points from a solitary balloon launch. Illustrative projects include the multidisciplinary analysis of the African  
65 monsoon and the measurement system research and forecasting experiments conducted in the Asia-Pacific  
66 region, which utilize balloons to conduct drop soundings as they drift with stable upper-air winds over the  
67 ocean (Raman et al., 2011; Johnson et al., 2024). Similarly, the Centre National d'Etudes Spatiales (CNES) of  
68 the French Space Agency, has developed a Super Pressure Balloon (SPB) capable of floating in the stratosphere  
69 for over three months (Roth et al., 2022). Additionally, the Tata Institute of Fundamental Research Balloon  
70 Facility (TIFR-BF) in India has also contributed to this field by developing comparable systems (Anand et al.,  
71 2021; Vernier et al., 2018; Vernier., 2022). Early stratospheric balloon systems encountered doubts concerning  
72 their long-term feasibility for operational data collection, attributable to cost and ascent rate limitations (WMO-  
73 No. 8., 2025). Additionally, slower ascent rates result in radiative errors issue. However, for wind vectors,  
74 especially crucial upper-level winds, GPS-based positioning provides high-precision data less affected by the  
75 ascent rate. The development of a new generation of commercial balloon systems has been changing this  
76 landscape. Studies by Ratnam et al., 2014 and Ingleby et al., 2022 looked at the quality and value of radiosonde

删除[CMA MOC luo]: Dropsonde data assimilation has been shown to hurricane trajectory forecast errors associated with an approximate reduction of 10-15% in specific contexts, such as short-term (0-48h) predictions over ocean basins using the GFS model, as demonstrated in multi-year statistical analyses( Ingleby, 2021; Cohn et al., 2013; Wang et al., 2015)

删除[CMA MOC luo]: While early stratospheric balloon systems faced questions about their long-term feasibility for operational data collection due to cost and ascent rate limitations (WMO-No. 8., 2025). For temperature and humidity, slower ascent can reduce the accuracy of vertical resolution due to issues like sensor response time and radiative errors.

删除[CMA MOC luo]:

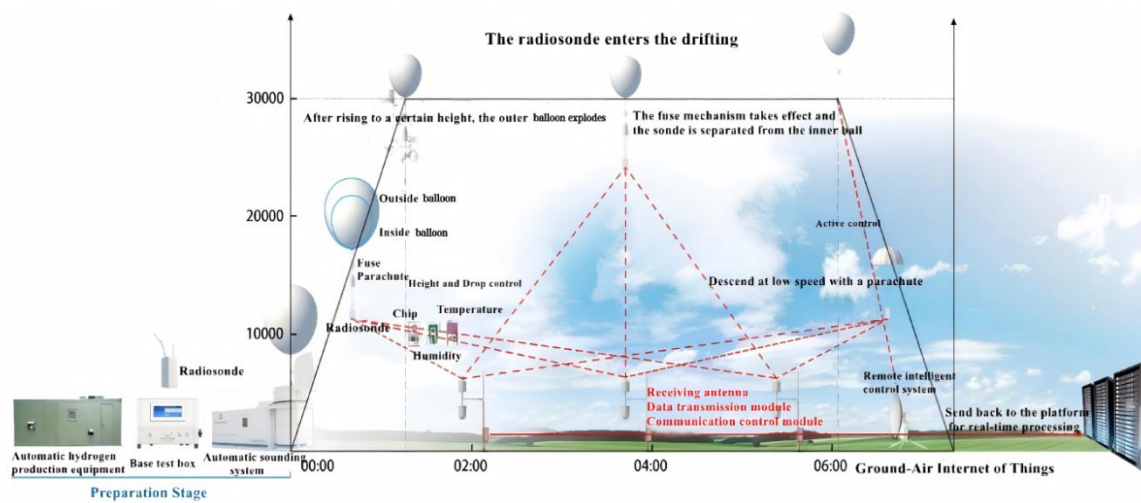
77 | descent data. This paper introduces a new sounding technology—the Ascent-Drift-Descent Radiosonde System  
 78 | (ADDRS). This system can improve the spatial and temporal frequency of soundings and provides an additional  
 79 | vertical profile as well as maintaining cost-effective, which acquires radiosonde measurement data throughout  
 80 | three phases—'Ascent-Drift-Descent' (ADD)—all with a single balloon launch (Cao et al., 2019; Cao et al.,  
 81 | 2022).

删除[CMA MOC luo]: (Ratnam et al., 2014; Ingleby et al., 2022)  
 删除[CMA MOC luo]: On account of the sounding process of ascending and descending at the same station has restricted its potential in conducting adaptive or targeting observation on typhoon forecast (Tan et al., 2006).

## 82 | 2. Synopsis of the Ascent-Drift-Descent Radiosonde System (ADDRS)

83 | The ADDRS was developed by the Meteorological Observation Centre of the China Meteorological  
 84 | Administration (MOC of CMA) with other relevant organizations in China (hereinafter referred to as the  
 85 | 'ADDRS research team'). It undertakes a three-phase upper-air measurement (Fig. 1).

删除[CMA MOC luo]: In addition to the ascent phase of the current sounding system, ADDRS enables sounding during both the drift and descent phases. This innovative approach completes three phases of sounding with only a single balloon launch, representing a significant advancement in comparison with the traditional upper-air sounding method that has been utilized for nearly a century (Cao et al., 2022).



86 |  
 87 | **Figure 1. Pre-operational principle diagram of the Ascent-Drift-Descent Radiosonde System (ADDRS).**

88 | **Table 1. Main instruments and key functions of ADDRS.**

No	Subsystem	Instruments	Key Function
1		dual-mode balloon	'outer balloon' as ascent carrier, 'inner balloon' as drift carrier
2	'ADD' subsystem	parachute	parachute as the carrier of the descent phase
3		drifting controller	Adaptive control of drift and descent
4		radiosonde	The temperature, pressure, humidity, wind measurement meet the demand for long-term stratospheric observation
5	Ground operation control subsystem	<u>Launch station</u>	<u>Manned radiosonde inspection, ground check, balloon inflation, and other balloon tasks.</u>
6		Multichannel sounding receiver	8 channels receive radiosonde data simultaneously
7		control command transmitter	<u>In a weather-sensitive area without a station, the inner balloon can be detached and the descent started.</u>
8		operation management system	Real-time acquisition, transmission, quality control, and timely delivery of control instructions for ADDRS data, providing real-time high-quality data to weather analysis and numerical prediction models

删除[CMA MOC luo]: ground  
 删除[CMA MOC luo]: Ground  
 删除[CMA MOC luo]: launch,  
 删除[CMA MOC luo]: before the equipment is launched  
 删除[CMA MOC luo]: In the weather-sensitive area without a station, the active fusing drifting controller is carried out and the descent measurement is started  
 删除[CMA MOC luo]: al

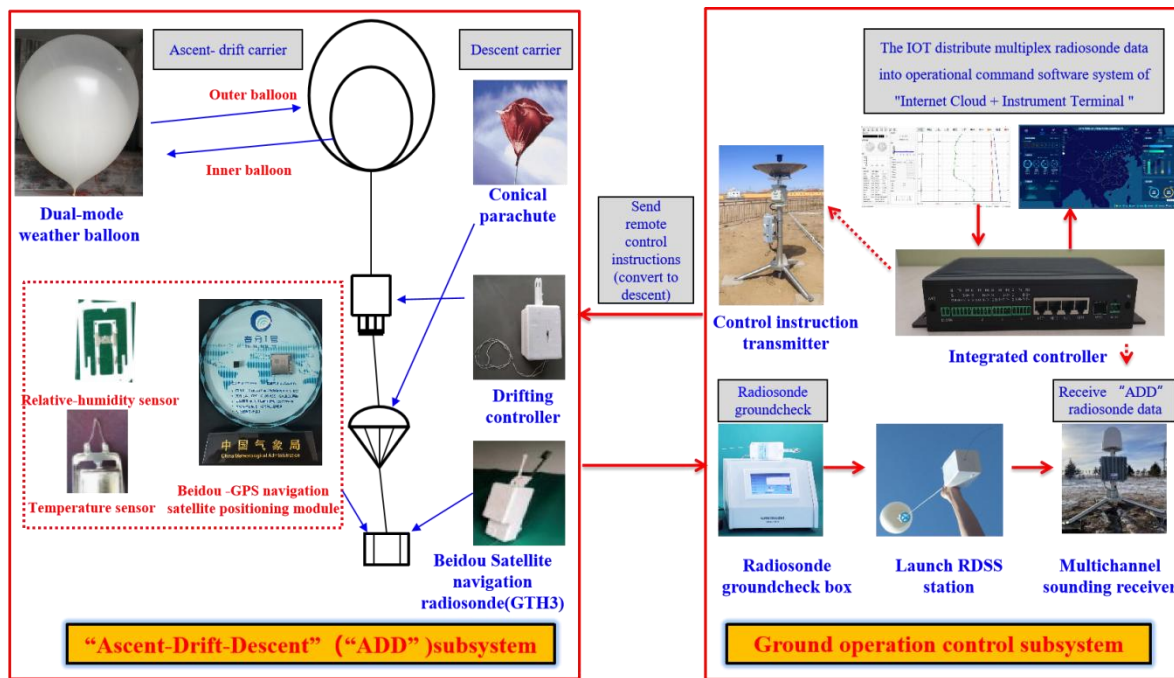


Figure 2. Schematic representation of the equipment composition for ADDR.

The ADDR primarily consists of the 'ADD' subsystem and the ground operation control subsystem, as shown in Table 1 and Fig. 2. The 'ADD' subsystem encompasses a dual-mode balloon with a parachute, a drifting controller, and a radiosonde. The dual-mode balloon features a design where one balloon embedded within another, both made from a latex material similar to that of meteorological sounding balloons and filled with hydrogen. Upon inflation and launch of the dual-mode balloon, the 'ADD' subsystem ascends at a rate of ascent between 5 and 7 m/s (WMO-No. 8., 2025). As it rises, the external air pressure decreases, causing the balloon to expand. At the predetermined altitude (generally between 28km and 30km), the outer balloon bursts due to its expanding volume, marking the conclusion of the ascent phase measurement. Given that the outer balloon bursts within the stratosphere, where vertical air movement is minimal, horizontal movement becomes predominant. The inner balloon, does not burst, and the buoyancy of the inner balloon attains equilibrium with vertical stability, starting the drift phase.

After drifting for a predefined duration, which may vary from a couple of hours to over ten hours, the drifting controller separates the inner balloon from the rest of the ADDR equipment, thereby terminating the drift phase. The parachute is promptly deployed, facilitating the radiosonde in collecting data during the descent phase, while acting as its carrier. This descent persists until the equipment touches down, thereby completing the final phase of the 'ADD' process. At this point, ADDR has successfully completed the three-phase 'Ascent-Drift-Descent' measurement.

The ground operation control subsystem of ADDR comprises four main components in Table 1. The launch station operates with a high degree of automation for scheduled sequences, though the critical procedure for inflating the inner balloon to achieve drift requires operator supervision. Full automation of this process is under active development. Ground data-receiver can also be placed at the balloon launch station. However, its layout and function differ from the operational-ground data-receiver. Due to the ADDR drift phase, the horizontal distance between the descent point of the radiosonde and its launch point can exceed 500km, while radiosonde data reception has a maximum linear transmission distance of around 200km-300km.

删除[CMA MOC luo]: al

删除[CMA MOC luo]: operational

删除[CMA MOC luo]: enable it to resist bursting.

删除[CMA MOC luo]: And the buoyancy

删除[CMA MOC luo]: Meanwhile, the remaining components—comprising the parachute and radiosonde—begins to descend.

删除[CMA MOC luo]: , including the balloon launch station, ground data-receiver (downlink communication), control command transmitter (uplink communication), and the operational management system

删除[CMA MOC luo]: balloon

删除[CMA MOC luo]: is

删除[CMA MOC luo]: similar to existing meteorological radiosonde launch station, undertaking tasks such as ground checks, balloon inflation, and launching the balloon with a radiosonde at scheduled intervals

删除[CMA MOC luo]: operational

115 Therefore, the traditional single-station, point-to-point radio communication mode of radiosondes is inadequate  
116 for ADDRS data reception. Thus, the ground to upper-air communication system has been upgraded from point-  
117 to-point to a multiple-to-multiple model. In areas through which the radiosonde's ADD phases may pass, ground  
118 data-receivers are strategically deployed. This configuration enables multiple ground data-receivers to  
119 concurrently receive data from a single radiosonde or alternatively, a single receiver to capture data signals from  
120 several radiosondes simultaneously. Consequently, the ground data-receiver is designed as a P-band 8-channel  
121 parallel data receiver, capable of receiving data from multiple radiosondes simultaneously. Additionally, control  
122 command transmitters are located at the ground station and other locations. These transmitters send control  
123 instructions from the ground to the drifting controller in the air through uplink communication. This system  
124 allows for the adjustment of the drift phase elevation, termination of the drift phase, and switching to the descent  
125 phase measurement as needed.

126 The operation management system acts as the brain of the entire ADDRS system. Multiple ground data-  
127 receivers and control command transmitters are connected to the operation management system by the Internet.  
128 These ground data-receivers continuously transmit data to the operation management system in real-time for  
129 processing, display, and storage. Based on the ADDRS trajectory and specific weather and climate conditions,  
130 comprehensive decision-making allows the operation management system to transmit control instructions to  
131 control command transmitters which then relay them to the drifting controller in the air to execute the desired  
132 functions.

删除[CMA MOC luo]: al

删除[CMA MOC luo]: al

删除[CMA MOC luo]: al

删除[CMA MOC luo]: al

133 The 'Internet cloud + Instruments terminal' architecture enables real-time, efficient, and bidirectional  
134 communication across the entire network during the 'ADD' phases. This configuration supports the seamless  
135 real-time acquisition, transmission, and quality control of ADDRS data while ensuring rapid data delivery for  
136 weather forecasting. Consequently, it enhances the timeliness and availability of radiosonde data for forecasting  
137 purposes.

### 138 3. Critical scientific problems

#### 139 3.1. Carrier technology

##### 140 3.1.1 Study on the influence of atmospheric environment on the net lift power of balloons

141 A multitude of meteorological factors, encompassing air temperature, air pressure, solar radiation, and  
142 other external environmental conditions, coupled with the gas volume of the outer balloon directly influences  
143 its net lift and burst altitude. Variations in pressure and temperature within the outer balloon, induced by  
144 external meteorological conditions, interact with the expansion dynamics of the inner balloon. These factors, in  
145 conjunction with the optimum volume of the inner balloon, collectively influence the altitude during the drift  
146 phase and the static equilibrium of the inner balloon. Consequently, controlling the hydrogen inflation volume in  
147 the dual-mode balloon presents a significant challenge.

删除[CMA MOC luo]: air

148 The ADDRS research team conducted an in-depth theoretical analysis of the ascent and drift processes of  
149 the dual-mode balloon, focusing on three areas: upper atmosphere model expansion, the balloon's dynamic  
150 equation, and a thermodynamic model. This study led to the development of a coupling model that accounts for  
151 the effects of atmospheric conditions on the balloon's net lift (from now on referred to as the 'coupling model')  
152 (Liu, S. J et al., 2022). This model provides a theoretical foundation for determining the net lift force, ascent

153 velocity, and target burst altitude of the dual-mode balloon, enabling precise control of the mass of air in the  
 154 balloons in the dual-mode balloon under varying meteorological conditions.

155 **Table 2. Inflate test results based on coupling model.**

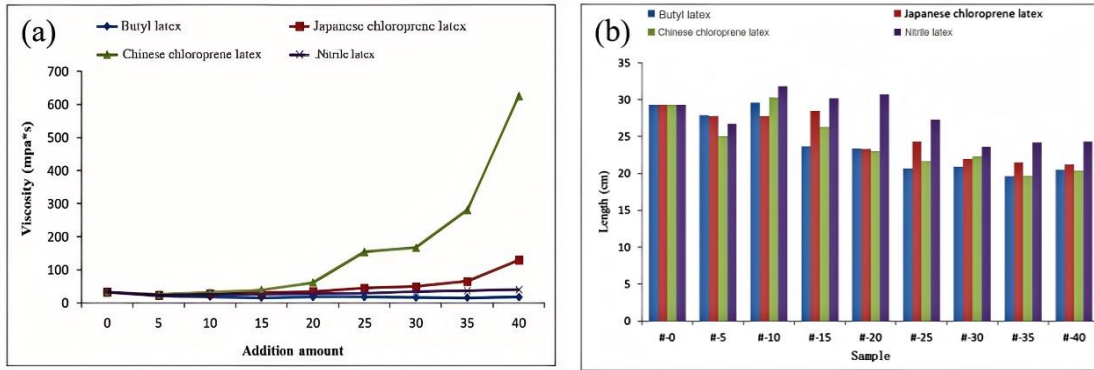
Inflatable mode	Effective launch times	Drift number of times	Drift success rate	$\geq 4h$ number of times	$\geq 4h$ success rate
Algorithm software	611	479	78.40%	436	71.36%

156 Table 2 presents data from six stations (Changsha, Wuhan, Anqing, Yichang, Nanchang, and  
 157 Ganzhou) situated along the middle and lower reaches of the Yangtze River in 2021. And based on the  
 158 sounding balloon observation data in Guangdong from August 2022 to October 2023, the optimum volume  
 159 capacities of related factors of the inner and outer balloons of the dual-mode sounding balloon on the success  
 160 rate of the drift were studied, and a reasonable inflation scheme was established to improve the success rate of  
 161 the drift. The research shows that the theoretical inflation amount of the inner balloon for drifting at the  
 162 expected height is 55.6 mol. Affected by day and night conditions, the inflation amount during the day should be  
 163 controlled at  $52.6 \pm 2$  mol, and at night, it should be controlled at  $57.6 \pm 2$  mol. The burst height of the outer  
 164 balloon has a significant impact on the success rate of the drift. When the burst height of the outer balloon is  
 165 within the expected height, the success rate of the drift can reach 82%. The success rate of the drift during the  
 166 day is higher than that at night, and the success rate under clear sky conditions is higher than that under cloudy  
 167 and rainy conditions. Under rainy conditions, the success rate of the drift is only 50.2%. After verification, the  
 168 success rate of the drift can reach 93.5% by adopting the reasonable inflation scheme (Xu et al., 2025).

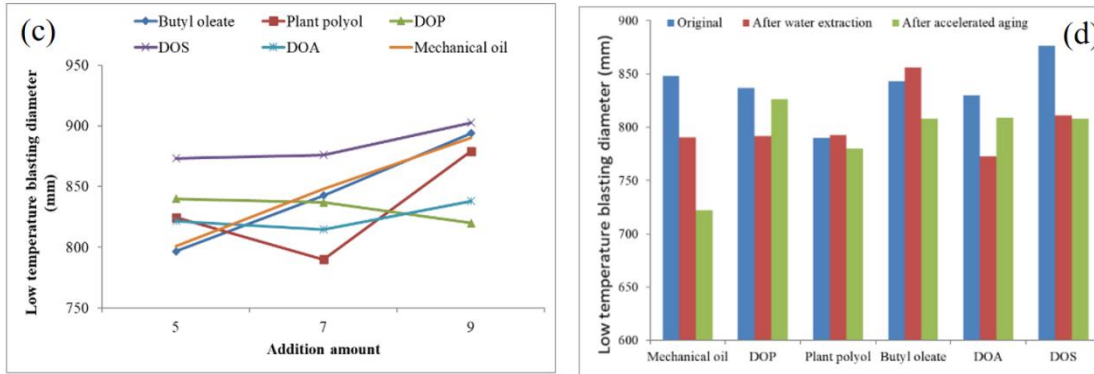
### 169 3.1.2 Performance improvement of the double - layer balloon

170 The ascent phase of meteorological sounding typically lasts between 1.5 and 2 hours. However, during the  
 171 ADD process, the inner balloon of the dual-mode balloon is exposed to low temperatures, intense ultraviolet  
 172 radiation, and high ozone concentrations for several hours or even up to ten hours. To address these challenges,  
 173 the ADDRS research team conducted formulation tests to enhance the inner balloon resistance to these  
 174 environmental factors, with a particular emphasis on natural latex modification, cold resistance, and anti-aging  
 175 systems. Considering that latex hot air aging performance improves air tightness and balloons are exposed to  
 176 prolonged sun exposure and hydrogen loss, the incorporation of a specific latex compound was found to  
 177 augment durability. Fig. 3a and 3b show that the addition of latex formulas had minimal impact on the latex  
 178 viscosity and the balloon appearance while improving its tensile strength and thermal aging resistance. Fig. 3c  
 179 and 3d demonstrate that butyl oleate exhibits the lowest reduction in low-temperature burst performance after  
 180 water extraction and accelerated aging, making it the best-performing cold-resistant agent. Consequently, this  
 181 agent was integrated into the formula to bolster cold resistance. For the anti-aging system, illustrated in Fig.3e  
 182 and 3f, nano zinc oxide, which can be diluted directly with water to replace traditional zinc oxide, was used.  
 183 Additionally, we incorporated antioxidants to enhance the balloons' resistance against ultraviolet and ozone  
 184 degradation. These formula improvements extend the inner balloon lifespan under harsh conditions of low  
 185 temperature, intense UV radiation, and high ozone levels. This enhanced durability has been applied to the inner  
 186 balloon, resulting in an extended service life and a high success rate during the drift phase (Zhu et al., 2021;  
 187 Shen et al., 2020).

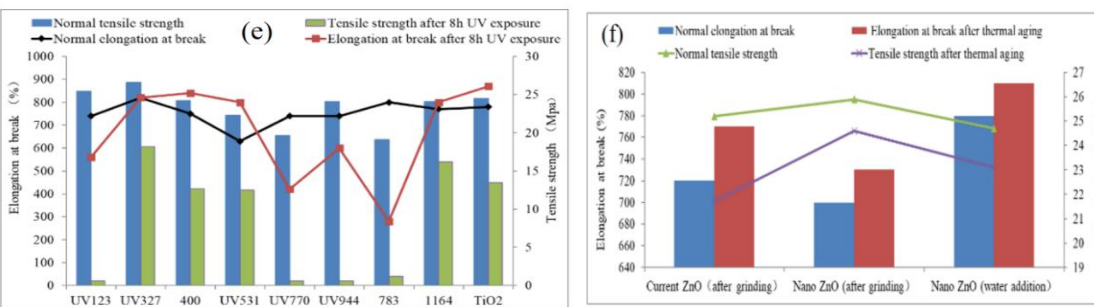
188



189



190



191 **Figure 3. Modification test of natural latex in the inner sphere:** (a) Four types of modified natural latex materials—  
 192 Butyl latex, Japanese chloroprene latex, Chinese chloroprene latex, and Nitrile latex—were screened and added to  
 193 natural latex using the homogenization method. (b) Physical properties of the modified natural latex pellet samples  
 194 were evaluated for operation and thermal aging tensile testing. (c) Butyl oleate, Plant polyol, DiOctyl Phthalate (DOP),  
 195 DiOctyl Sebacate (DOS), DiOctyl Adipate (DOA), and mechanical oil were added to natural latex as cold resistance  
 196 agents. Cold resistance system test: The blasting diameters of six types of cold-resistant samples were tested using low-  
 197 temperature blasting instruments at  $-85^{\circ}\text{C}$ . (d) Low-temperature blasting diameters were measured for six types of  
 198 raw, water-pumped, and aged samples with seven parts of cold-resistant agents added. Anti-aging system test: (e)  
 199 Comparison of tensile properties among nine anti-aging agents—UV327, UV400, UV531, UV1164, and TiO<sub>2</sub> filler—  
 200 with 0.2 parts of one-component anti-aging agent after eight hours of operation and ultraviolet aging. (f) Comparison  
 201 of tensile properties after ozone aging between Nano ZnO and ZnO.

删除[CMA MOC luo]: al

删除[CMA MOC luo]: d

删除[CMA MOC luo]: al

## 202 3.2 Payload technology

### 203 3.2.1 Performance improvement of the radiosonde

204 Due to ADDRS operates effectively across all three phases of the ADD process, requiring a minimum  
 205 operation time of six hours. This extended operation necessitates a larger-capacity battery for the ADDRS  
 206 radiosonde. Additionally, the radiosonde's weight affects the balloon's inflation volume, making it essential to  
 207 reduce the radiosonde's weight where possible. Therefore, an integrated, lightweight, and low-power radiosonde  
 208 is crucial, and the ADDRS research team developed a specialized SoC (System on Chip) module (named  
 209 Equinox I) for CMA's GTH type of Beidou-based radiosonde.

删除[CMA MOC luo]: The ADDRS payload unlike operational radiosonde,

删除[CMA MOC luo]: al

210 The GTH3 employs a specialized SoC module of meteorological sounding and utilizes a multi-layer board  
211 design and miniaturized components to reduce the size, weight, and power consumption. Compared to the  
212 previous operational radiosonde (GTS12 radiosonde, WMO BUFR code:201), the GTH3 radiosonde (WMO  
213 BUFR code:206) significantly reduce the overall size, weight, and power consumption of the device.  
214 Furthermore, the amount of plastic and toxic materials in the circuit boards has also been substantially reduced  
215 (Table 3).

216 The GTS12 and GTH3 radiosonde use the same PTU sensor, P(MEMS piezo-resistive), T(adopting self-  
217 developed NTC bead thermistor (reduced from diameter  $\leq 1\text{mm}$  to  $\leq 0.4\text{mm}$ ) volume reduction, higher  
218 sensitivity), U (capacitive thin-film polymer humidity sensor). The difference lies in that 'Instrumentation and  
219 Methods' :

220 For P [Design the temperature compensation circuit and establish the correction equation by fitting the  
221 sensor characteristic surface through multiple temperature segments and multiple pressure points to achieve  
222 higher measurement accuracy.]

223 For T [Optimize the installation structure, included Angle and lead length through simulation analysis, and  
224 effectively reduce the influence of solar radiation by improving the installation structure and coating process.]

225 For U [Optimize the Temperature compensation Correction Algorithm and humidity hysteresis Correction  
226 Algorithm for Humidity sensors]

227 The GTH3 participated in WMO UAH2022 (Upper-Air Instrument Intercomparison Campaign organized  
228 by the World Meteorological Organization (WMO) and co-organized by the Deutscher Wetterdienst (DWD) in  
229 2022) with the results shown in Table 4. It is suitable for applications in ORUC (Operational and Research Use  
230 in Climatology), including aeronautic meteorology, near/ultra-short-term forecasting, global numerical weather  
231 prediction, and real-time monitoring (WMO IOM-143., 2024).

删除[CMA MOC luo]: Besides

删除[CMA MOC luo]: compare to GTS12 radiosonde of L-band Secondary Wind-sounding radar ()

删除[CMA MOC luo]: ing

删除[CMA MOC luo]: ing

232 **Table 3. Comparison of parameters among RS41, GTH3 and GTS12 radiosonde.**

Radiosonde type	Positioning method	Volume (mm <sup>3</sup> )	Weight (g)	Transmitting power (mW)	Working time (min)	Data Transmission Rate(bps)	Battery Weight (g)	Foam Packaging Weight (g)	Circuit boards Weight (g)
GTS12 radiosonde	Radar positioning	190×90×245	<400	400≤	>120	1200	<250	<70	<80
GTH3	Equinox I	155×65×60	<120(for one profile)	100≤	>240	Optional,2400,4800,9600	<40	<30	<50
		155×65×60	<170(for “ADD” three phase profile)	100≤	>640		<90	<30	<50
Vaisala RS41	u-blox G7020	155×60×46	109	60	>240	4800	76	/	/

233 **Table 4. The evaluation results of GTH3 radiosonde temperature, pressure, relative humidity, wind and geopotential height in WMO Instruments and Observation Methods Report**  
 234 **No. 143. page.150(Note: The data are in the form of  $\Lambda_{c,L}^{\delta_{c,L} \pm \epsilon_{c,L}}$ , where  $\Lambda_{c,L}$  represents the individual measurement root mean square error,  $\epsilon_{c,L}$  denotes the measurement**  
 235 **uncertainty,  $\delta_{c,L}$  is the measurement error, and  $\sigma(\delta)$  indicates the measurement standard deviation. The planetary boundary layer (PBL) ranges from surface to 2 kilometers; the**  
 236 **free troposphere (FT) ranges from 2 kilometers to the tropopause 12 kilometers are in the ; the upper troposphere/lower stratosphere (UTLS) ranges from 7 kilometers to 17**  
 237 **kilometers; the middle and upper stratosphere (MUS) is above 17 kilometers up to the bursting point of the sounding balloon. )**  
 238

Time	Height	Atmospheric temperature [K]	Relative humidity [%RH]	Geopotential height [m]	Pressure [hPa]	Wind (horizontal)direction[°]	Wind (horizontal)speed [m.s <sup>-1</sup> ]	Wind (horizontal)vector [m.s <sup>-1</sup> ]
Day	PBL	$0.18_{0.17}^{-0.05} \pm 0.03$	$7.00_{4.41}^{-5.43} \pm 0.74$	X	X	X	X	X
	FT	$0.12_{0.11}^{+0.05} \pm 0.04$	$8.75_{8.02}^{-3.50} \pm 0.60$	$5.9_{5.5}^{+2.0} \pm 1.8$	$0.4_{0.4}^{-0.0} \pm 0.1$	$3.6_{3.6}^{-0.4} \pm 0.2$	$0.2_{0.2}^{-0.0} \pm 0.0$	$0.3_{0.1}^{+0.2} \pm 0.0$
	UTLS	$0.09_{0.08}^{+0.01} \pm 0.03$	$7.73_{7.58}^{-1.55} \pm 0.40$	$13.2_{8.6}^{+10.0} \pm 3.8$	$0.4_{0.2}^{-0.3} \pm 0.1$	$2.5_{2.5}^{-0.2} \pm 0.3$	$0.2_{0.2}^{-0.0} \pm 0.0$	$0.3_{0.2}^{+0.2} \pm 0.0$
	MUS	$0.27_{0.16}^{-0.22} \pm 0.10$	$1.69_{0.82}^{+1.48} \pm 0.46$	$29.5_{17.9}^{+23.4} \pm 4.2$	$0.3_{0.1}^{-0.2} \pm 0.0$	$6.1_{6.1}^{-0.4} \pm 0.2$	$1.3_{1.3}^{-0.0} \pm 0.0$	$1.5_{1.5}^{+0.3} \pm 0.0$
Night	PBL	$0.38_{0.34}^{-0.18} \pm 0.05$	$4.72_{4.66}^{+0.74} \pm 0.15$	X	X	X	X	X
	FT	$0.15_{0.15}^{+0.02} \pm 0.02$	$6.41_{6.03}^{+2.16} \pm 0.11$	$5.8_{5.8}^{+0.4} \pm 0.4$	$0.5_{0.5}^{+0.1} \pm 0.2$	$2.6_{2.6}^{-0.2} \pm 0.2$	$0.2_{0.2}^{-0.0} \pm 0.0$	$0.2_{0.1}^{+0.2} \pm 0.0$
	UTLS	$0.12_{0.10}^{+0.06} \pm 0.05$	$6.82_{5.74}^{+3.70} \pm 0.26$	$11.5_{8.6}^{+7.7} \pm 3.4$	$0.3_{0.2}^{-0.1} \pm 0.1$	$2.4_{2.4}^{-0.1} \pm 0.1$	$0.2_{0.2}^{+0.0} \pm 0.0$	$0.2_{0.1}^{+0.2} \pm 0.0$
	MUS	$0.10_{0.10}^{-0.03} \pm 0.02$	$1.71_{0.74}^{+1.54} \pm 0.28$	$26.7_{16.8}^{+20.7} \pm 4.2$	$0.1_{0.1}^{-0.1} \pm 0.0$	$4.5_{4.4}^{-0.6} \pm 0.2$	$0.2_{0.2}^{-0.0} \pm 0.0$	$0.4_{0.3}^{+0.3} \pm 0.0$

### 240 3.2.2 Drifting controller

241 The drifting controller can be considered part of the ADDRS payload. It connects to an inner balloon above  
242 and a parachute and radiosonde below. The controller fuses a wire with an instant high electric current,  
243 triggering the mechanical device to disconnect the parachute and the radiosonde. The controller serves two main  
244 functions during the drift phase:

- 245 1. Similar to the Windborne system, it is equipped with a ballast-dropping mechanism to control its weight,  
246 allowing the inner balloon to better adapt to changes in altitude.
- 247 2. Separate the inner balloon from the other sounding equipment (parachute and radiosonde). Moreover, the  
248 drifting controller can also initiate the fuse based on predetermined control rules, such as altitude limits  
249 ( $\leq 18$  km), specified time, the latitude and longitude of a designated area, or upon receiving commands  
250 from the ground. This action can be taken before the drifting balloon is about to enter the specified area or  
251 approach the maximum drift height. As a result, it will effectively end the drift phase, separating the  
252 parachute and radiosonde from the balloon.

### 253 3.3. Receiving radiosonde data and sending control instructions technology

254 The ADDRS ground data-receiver utilizes a high-gain, low-power, ultra-compact omnidirectional antenna,  
255 along with super-heterodyne architecture and multiple communication protocol algorithms, including time  
256 division multiple access, frequency division multiple access, and code division multiple access (Gong et al.,  
257 2021). It supports various frequency modulation modes and achieves a receiving sensitivity of better than -120  
258 dBm (at 2400 bps), effectively addressing self-interference issues in multi-channel radiosonde data reception.  
259 Additionally, the system incorporates narrow-band wireless communication technology to improve low-  
260 elevation reception when the radiosonde drops below the receiving antenna's height, facilitating broad-area  
261 coverage with a visual range radius for upper-air coverage of at least 200 km. The receiver can adapt to diverse  
262 application scenarios, such as fixed stations, vehicles, and ships. With an average data reception rate of 99.7%,  
263 the ground receiver at the Anqing station has demonstrated an impressive maximum reception distance of up to  
264 487 km.

265 Unlike the one-way (downlink) communication mode used in [radiosonde](#) systems, the ADDRS control  
266 command transmitter can send ground instructions to the drifting controller, with a linear communication range  
267 extending beyond 300 km. This capability allows for precise control over the drifting controller to execute  
268 actions such as releasing counterweights or separating the balloon from the parachute and radiosonde, enabling  
269 the radiosonde to conduct drift phase measurements within the target area (Liu et al., 2021). During field tests,  
270 over ten balloon discharge control commands were successfully transmitted, with the farthest reaching 403 km.

| 删除[CMA MOC luo]: operational sounding

### 271 3.4. 'ADD' measurement technology

272 The details of the ADD measurement method are outlined by (Cao et al., 2019). The ascent phase  
273 measurement technique adheres to the guidelines outlined in the CMA technical specification. The primary  
274 research focus of the ADDRS is on the measurement techniques for the drift and descent phases.

#### 275 3.4.1 Temperature measurement method in the drift phase

| 删除[CMA MOC luo]: flat

276 During the drift phase of ADDRS, the inner sphere of the dual-mode balloon moves with the horizontal  
277 airflow in the stratosphere. The radiosonde's vertical movement, with the surrounding atmosphere, is minimal  
278 and it can be approximately considered as drifting with the horizontal wind. The effect of radiation on the  
279 temperature sensor during this phase is greater than during the ascent and descent phases, leading to  
280 considerable measurement errors that are challenging to correct using general quality control algorithms.

281 Given the unique conditions of stratospheric air temperature measurement, the ADDRS research team  
282 employs a multi-physical field, fluid-structure coupled computational fluid dynamics (CFD) approach to model  
283 the behavior of the temperature sensor in high-altitude, low-wind-speed environments. This model calculates the  
284 flow and the temperature field, accounting for radiation effects based on sun elevation, ventilation, sensor size,  
285 and surface reflectivity. To ensure broad applicability, neural networks, and other mathematical methods are  
286 used to fit the extensive simulation data, yielding practical error-correction equations (Yang et al., 2014).

287 Considering that there may be discrepancies between CFD simulations and real environmental conditions,  
288 the ADDRS research team uses instruments such as low-pressure wind tunnels and solar simulators to create an  
289 experimental platform. This setup simulates ventilation, air density, and solar radiation conditions during the  
290 drift phase, allowing for the measurement of temperature errors due to solar radiation. These measurements  
291 verify and refine the simulation-based error correction equations (Yang et al., 2022).

### 292 3.4.2 Vertical wind data during the parachute descent

293 Currently, due to the pendulum effect, vertical wind measurements cannot be performed in balloon-borne  
294 soundings. The parachute-drop wind measurement model established by the WMO and NCAR does not address  
295 vertical wind measurement directly (Wang et al., 2015), instead assuming a zero vertical wind speed. This  
296 model assumes that the parachute-drop system is influenced only by gravity and vertical resistance, omitting  
297 other factors like buoyancy, additional forces, and parachute rotation during descent. This limitation prevents  
298 the analysis of vertical wind and also affects the accuracy of horizontal wind field calculations (Ingleby et al.,  
299 2022).

删除[CMA MOC luo]: Jensen et al., 2010;

300 Therefore, the ADDRS research team developed a more comprehensive vertical wind measurement model  
301 by considering all relevant forces acting on the balloon-launched and parachute descent dropsonde system,  
302 utilizing the domestic Beidou-based radiosonde, shows significant promise. The Beidou-based radiosonde  
303 demonstrated acceptable accuracy during both ascent and descent phases compared to the RS92 standard. The  
304 key advantages identified were the ability to perform temporally intensive sounding observations (effectively  
305 obtaining an 'ascent' and 'descent' profile from one launch) and the potential to spatially expand coverage  
306 through the drift of the parachute, allowing for a 'one-station launch, multi-station reception' model. This  
307 technology aligns with the trend towards automated, quantitative remote sensing in meteorological observation  
308 (Guo et al., 2018). The string length between the balloon/parachute and the GTH3 radiosonde is standardized at  
309 30 meters in manual launches. This length helps reduce sensor exposure to balloon wake effects but amplifies  
310 pendulum motion in wind data. More than ten comparative tests were carried out for the selection of the conical  
311 parachutes. The oscillation angle of conical parachute is less than 1°, which can ensure the rationality of the  
312 Gaussian filtering correction filter window for the horizontal wind in the descent phase. Meanwhile, a larger  
313 main parachute size can reduce the descent speed. Therefore, without considering the cost, a 'large conical  
314 parachute' is recommended for the descent phase detection of ADDRS. And make sure the parachute area

删除[CMA MOC luo]: Comparative tests led to the selection of conical parachutes to minimize swing effects on measurements.

删除[CMA MOC luo]: And carried out m

删除[CMA MOC luo]:

315 should be tailored to match the radiosonde weight. The descent phase of ADDRS could achieve a low-level  
316 descent speed of  $6 \text{ m/s} \pm 1 \text{ m/s}$  can be achieved in UTLS (upper troposphere and lower stratosphere (7-17km),  
317 and a swing angle below  $5^\circ$ , as well as a vertical wind measurement uncertainty of less than 1 m/s. These  
318 findings demonstrate that the model is effective for calculating vertical wind.

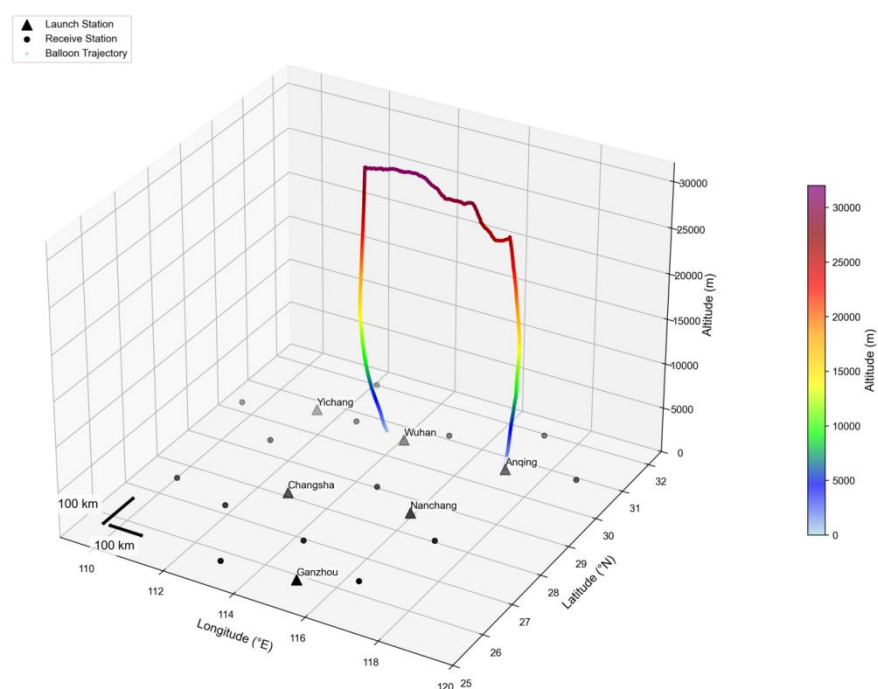
设置格式[CMA MOC luo]: 字体: 10 磅, 字体颜色: 自动设置

删除[CMA MOC luo]: is

## 319 4. Field experiments and data quality verification

### 320 4.1. Field experiment in the middle and lower reaches of the Yangtze River Region

321 From 2019 to 2021, ADDRS conducted field tests and application research across a wide area in the middle  
322 and lower reaches of the Yangtze River in China. The research focused on measurement data processing  
323 methods, quality control algorithms, and application technologies across diverse scenarios. The ADDRS  
324 radiosondes were launched from six stations. They were Anqing, Wuhan, Yichang, Nanchang, Changsha, and  
325 Ganzhou, which located in Anhui, Hubei, Jiangxi, and Hunan provinces. A total of 14 ground radiosonde data  
326 receivers were strategically positioned around these six stations, spaced approximately 150 km apart. The test  
327 covered an area of 600,000 square kilometers, as shown in Fig. 4, and show a trajectory for ADDRS at the  
328 Anqing station at 12:00 UTC on 11 July 2021.



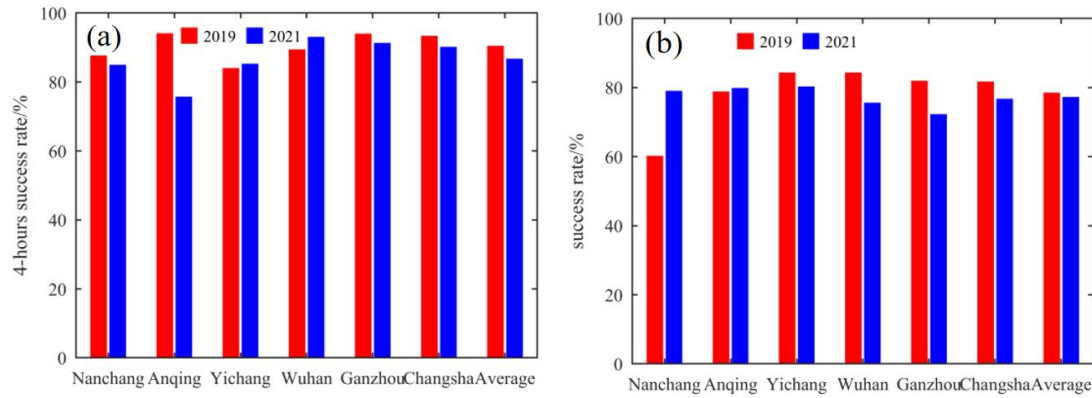
329 **Figure 4. The network distribution of ADDRS and an example of measurement: the trajectory for ADDRS at the**  
330 **Anqing station at 12:00 UTC on 11 July 2021. The black triangles represent balloon launch stations of ADDRS , while**  
331 **the black dots represent ADDRS receiving stations.**

删除[CMA MOC luo]: e radiosonde data

333 During the 13-month experimental period, 3,177 ADDRS launches were conducted, with 3,012 classified  
334 as effective launches, of which 2,369 achieved successful drifting. Among these, 2,136 launches resulted in  
335 drifting for more than 4 hours. The overall drifting success rate was 79%, with a 4-hour drifting success rate of  
336 71% (Fig. 5).

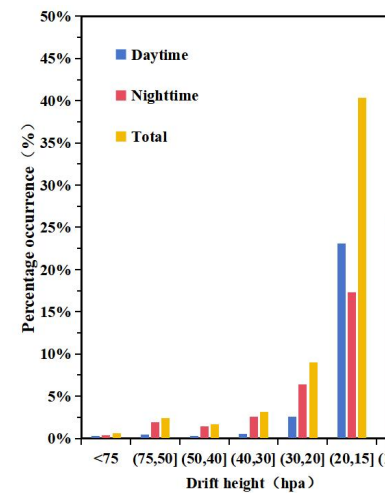
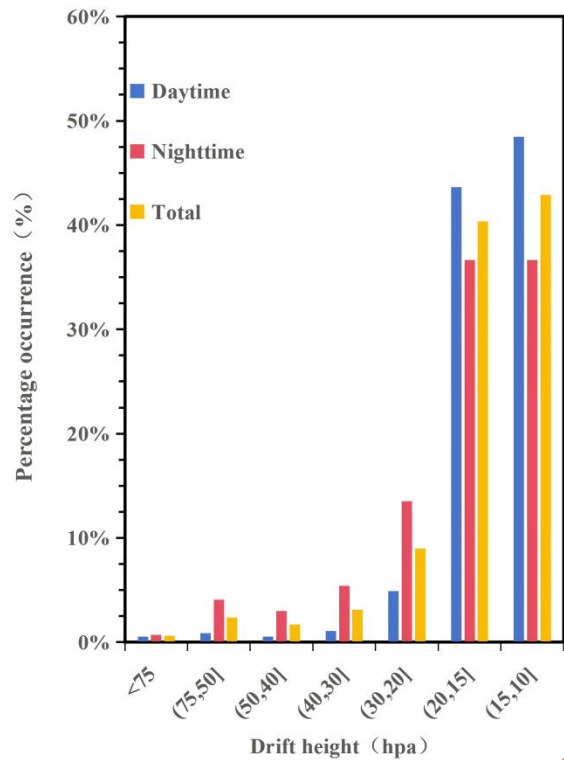
删除[CMA MOC luo]: of ADDRS

337



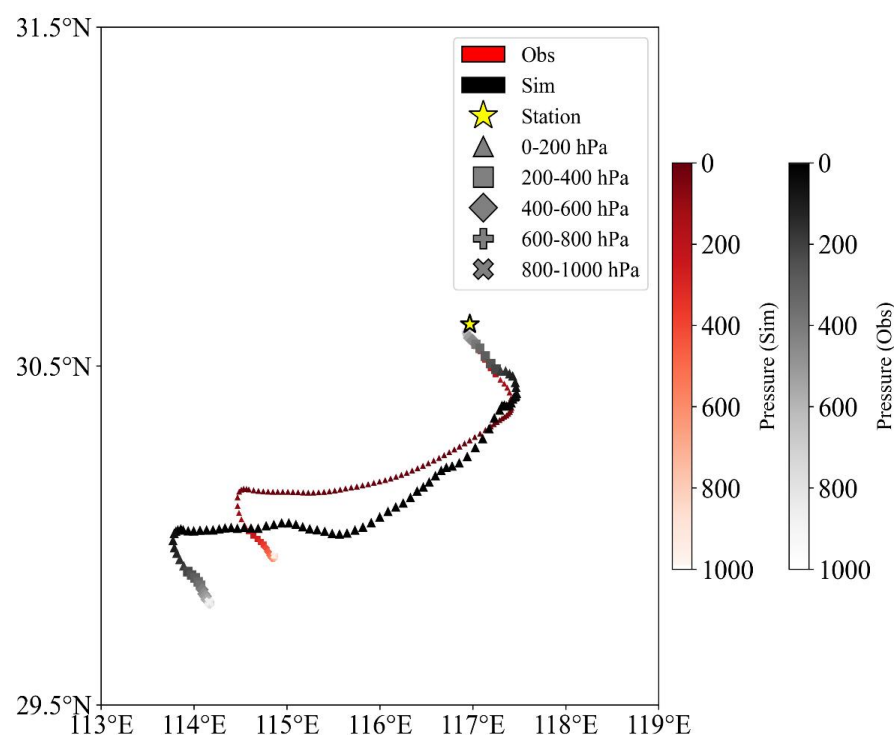
338  
339 **Figure 5. The field experiment in the middle and lower reaches of the Yangtze River Region (2019-2021): (a) Drifting**  
340 **success rate; (b) 4-hour drifting success rate.**

341 From March to September 2021, 2,427 'ADD' radiosonde launches were conducted, with 2,281 classified  
342 as effective launches, of which 1,772 achieved successful drifting. Among these, 1587 launches resulted in  
343 drifting for more than 4 hours. The overall drifting success rate was 78%, with a 4-hour drifting success rate of  
344 70%. The 1,772 successful drifts were analyzed (Fig. 6), and 937 were successful during the daytime,  
345 accounting for 53%. The successful nighttime drifting was 835 times, accounting for 47%, somewhat worse  
346 than the daytime performance. The drift heights ranging from < 75hPa (<18km) to 15hPa-10hPa (28km-32km)  
347 were statistically analyzed. The proportion of outer balloon explosion heights within 15hPa-10hPa (28km-32km)  
348 was the largest (43%). And the proportion of 20hPa-15hPa (26km-28km) is 40%, the proportion of 30hPa-  
349 20hPa (24km-26km) is 9%, and the total proportion of beyond 30hPa is 92%. Therefore, The drift height meets  
350 the GBON requirement of attaining at least 30hPa for a majority of ascents, with a subset of ascents also  
351 reaching the 10hPa level (WMO, 2020).



352  
353 **Figure 6. The drifting height of sounding-forecasting interactive network experiment (2021): (a) drifting height; (b) descent height**

354 Due to the limited availability of high frequency, continuous measurement data for the stratospheric  
 355 atmosphere, experiments were conducted in the middle and lower reaches of the Yangtze River to obtain direct  
 356 measurement data with high spatial and temporal density (Zhang et al., 2021). The simulated and observed  
 357 trajectories are represented by red and black, respectively (Fig. 7). A color gradient based on pressure altitude is  
 358 used to indicate the variation of trajectory height along the path.



359  
 360 **Figure 7. Schematic diagram of the observed (black) and simulated (red) trajectories. The yellow pentagram**  
 361 **indicates the radiosonde station. The color of each point represents the corresponding pressure level. Distinct**  
 362 **markers are used every 200hPa to enhance visual differentiation.**

363 The balloons drifting of ADDRS radiosondes data in the above [tropopause](#) have been very useful for  
 364 verification of FY-3D satellite temperature and humidity profiles (Zhou et al., 2023; Zhou et al., 2024). And  
 365 application in observing certain features of gravity waves in the lower stratosphere (He et al., 2024; Yang et al.,  
 366 2021) and feature extraction and analysis of atmospheric turbulence (Yang et al., 2023).

#### 367 4.2 Data quality evaluation

368 Aiming at the characteristics of high-resolution ADDRS data for quantitative application, the ADDRS  
 369 research team carefully evaluated ADDRS data using 31 data quality control methods based on the guidelines  
 370 for CMA technical specification of operation, upper-air meteorological observation (Wang, D et al. 2020). For  
 371 the data quality of the ascent phase of the ADD radiosonde, refer to the results in Table 4. Additionally, the  
 372 fifth generation of ECMWF (ERA5) global reanalysis (Hersbach et al., 2020) was used to evaluate the quality of  
 373 four upper-air radiosonde observations stations' ADDRS data in Guangdong (Zhang, C.Z et al., 2025), and  
 374 [Table 5 demonstrates good consistency between the ascent and descent phases for temperature, u-wind, and v-](#)  
 375 [wind](#) (Yao et al., 2026). The conclusion is basically consistent with the results of Table 4.

删除[CMA MOC luo]: al

删除[CMA MOC luo]:

删除[CMA MOC luo]: Table 5 shows the results of field experiment in the middle and lower reaches of the Yangtze River Region (Yao et al., 2026). The standard deviation results of ascent phase compared with descent phase (temperature, u-wind, v-wind) show good consistency

376 But for relative humidity (RH), different radiosonde manufacturers may adopt distinct saturation vapour  
 377 pressure (SVP) equations in calibrating humidity sensors. This difference in the choice of SVP equation can lead  
 378 to discrepancies in relative humidity measurements among different radiosonde types, especially under low-  
 379 temperature conditions. The ADDR5 radiosonde humidity sensor is calibrated using the Goff (1957) SVP  
 380 equation recommended in earlier WMO publications (WMO, 2012). Moreover, relative humidity from the  
 381 ERA5 dataset is calculated using the Buck SVP equation. To ensure a more consistent comparison, relative  
 382 humidity was recalculated from temperature and specific humidity in the ERA5 dataset using the Goff (1957)  
 383 SVP equation, with the SVP assumed over liquid water only. The results show that the O–A bias and RMSE of  
 384 relative humidity under low-temperature conditions are reduced and become much more physically reasonable.

385 The wind data from the drift phase were validated through dedicated experiments involving accelerometers,  
 386 applying filtering principles consistent with Marlton et al. (2015). However, we note that the discrepancies in  
 387 the stratospheric drift phase (both wind and temperature) are larger. This is consistent with findings from other  
 388 studies comparing high-resolution radiosonde data with reanalyses (Pauley and Ingleby, 2022; Ingleby, 2017).  
 389 such differences are often attributed to representation errors arising from the inherent resolution mismatches.

390 A known warm bias, correlated with high initial descent rates (frequently >50 m/s), affects temperature  
 391 measurements during the early descent (Ingleby et al., 2022). Consistent with operational practice, data from the  
 392 initial high-descent-rate period in this study were filtered out prior to the comparison with reanalysis data  
 393 presented. This quality control step mitigates the impact of this bias on the statistical results.

394 **Table 5. Comparative analysis of after-quality control of ADDR5 radiosonde data and ERA5 (O-A).**

			U (m/s)		V (m/s)		T (K)		RH (% RH)	
			bias	std	bias	std	bias	std	bias	std
Ascent	Day	Above <u>tropopause</u>	0.03	1.73	0.11	1.91	-0.4	1.04	/	/
		Below <u>tropopause</u>	0.13	1.41	0.08	1.47	0.04	0.69	1.32	8.57
	Night	Above <u>tropopause</u>	-0.02	1.72	-0.01	1.87	0.01	1.02	/	/
		Below <u>tropopause</u>	0.13	1.4	0.02	1.46	0.08	0.66	1.62	8.32
Drift		Above <u>tropopause</u>	/	3.32	/	3.22	/	3.09	/	/
Descent	Day	Above <u>tropopause</u>	0.16	1.74	-0.02	1.9	0.9	1.14	/	/
		Below <u>tropopause</u>	0.14	1.65	0.01	1.7	0.42	0.75	-1.7	10.12
	Night	Above <u>tropopause</u>	0.16	1.73	0.03	1.84	0.21	1.06	/	/
		Below <u>tropopause</u>	0.15	1.67	0.05	1.67	0.04	0.73	0.5	10.47

## 395 5. Application of ADDR5 in numerical forecasting techniques

### 396 5.1 A case study of weather analysis

397 Through long-term testing, the ADDR5 have the potential to capture key information in convective system  
 398 monitoring. From July 8 to 9, 2021, a strong convective weather event with a long duration and a large impact  
 399 area occurred in the middle and lower reaches of the Yangtze River in China. Convection developed and moved  
 400 to northern Jiangxi, northern Zhejiang, southern Anhui, and southern Jiangsu overnight on July 8 (Fig.8). The  
 401 drifting trajectories of ADDR5 radiosondes were from west to east, which aligned with the movement and

删除[CMA MOC luo]:

删除[CMA MOC luo]: We also note that the discrepancies between the measured wind and temperature data during the drift phase and the ERA5 reanalysis data are significantly larger, a phenomenon consistent with most radiosonde data comparisons at high altitudes (typically above 300hPa) against ERA5 (). With the continued accumulation of continuous drift phase of ADDR5 data in the future, it holds the potential to support research and improvements in reanalysis datasets like ERA5.

删除[CMA MOC luo]: .

删除[CMA MOC luo]: the temperature 'descent' warm results represents a noteworthy issue for future research.

删除[CMA MOC luo]: troposphere

删除[CMA MOC luo]: troposphere

删除[CMA MOC luo]: troposphere

删除[CMA MOC luo]: troposphere

删除[CMA MOC luo]: troposphere

删除[CMA MOC luo]: troposphere

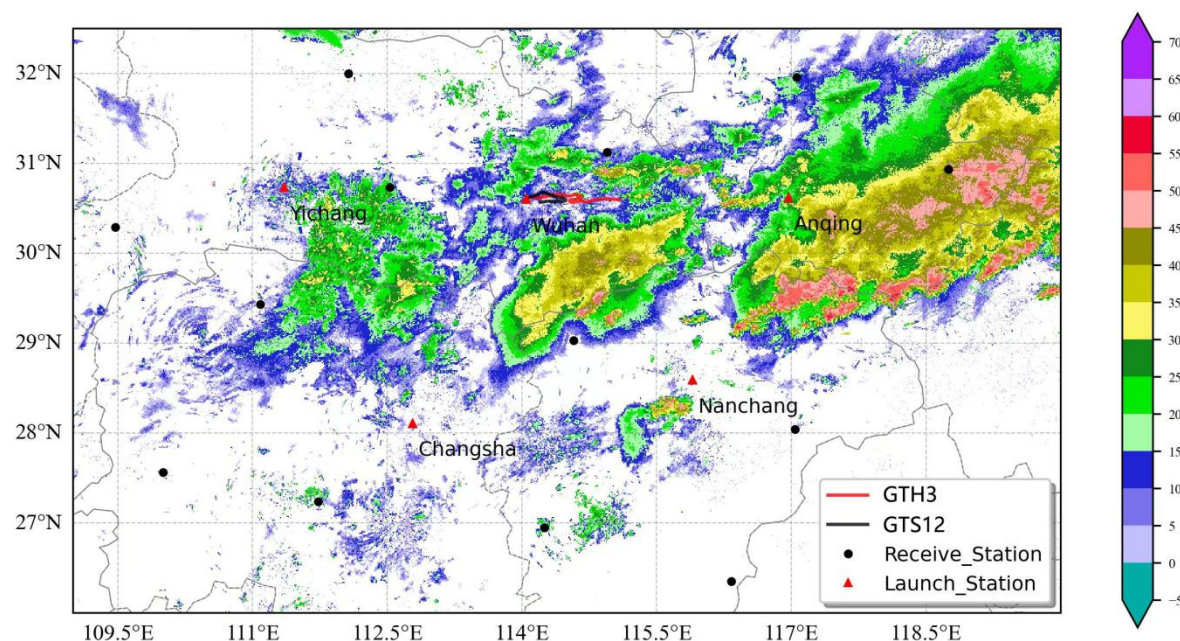
删除[CMA MOC luo]: troposphere

删除[CMA MOC luo]: troposphere

删除[CMA MOC luo]: troposphere

删除[CMA MOC luo]: for

402 development direction of severe convection. The descent phase radiosondes of ADDRS provides effective  
403 monitoring and insights in tracking the occurrence of the convective system and the changes in the ambient field.



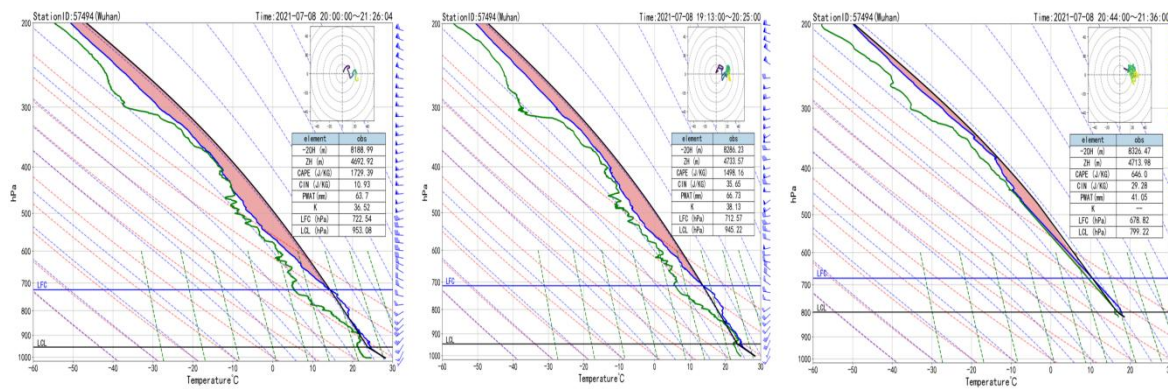
404

405 **Figure.8 The trajectory for GTH3 and GTS12 radiosonde at the Wuhan station and radar reflectivity image at 12:00**  
406 **UTC on 8 July 2021.**

407 Figure 8 displays the trajectory data of the ADDRS and GTS12 radiosondes launched from the Wuhan  
408 Meteorological Station. On the night of 8 November, at 11:15 UTC, Wuhan was situated on the western flank of  
409 the main convective system. The ADDRS radiosonde was launched at this time from the station, followed by the  
410 GTS12 radiosonde at 12:00 UTC from the same location. During the ascent phase, the curve of the ADDRS  
411 radiosonde (Fig. 9b) exhibited a trend similar to that of the GTS12 (Fig. 9a). A comparison of the ascent-phase  
412 data revealed that the convective available potential energy (CAPE) values differed between the two instruments  
413 as convection developed. The GTS12 measured a CAPE of 1729.39 J/kg at 12:00 UTC, higher than the value of  
414 1498.16 J/kg recorded by the ADDRS at 11:15 UTC.

415 Influenced by an upper-level westerly jet, the ADDRS sounding balloon drifted eastward toward the  
416 Wuhan. At 13:30 UTC, ADDRS conducted descent phase measurements (Fig. 9c). As shown in the layer curve,  
417 the CAPE value at 21:30 decreased compared with that at 12:00 UTC, dropping to 646.0J/kg, which was lower  
418 than the energy recorded at the Wuhan station. There is still a westerly jet stream with wind speed greater than  
419 20m/s beyond the upper-air of 500hPa level. The east of Wuhan proximity to the main body of convection, the  
420 reduction in energy suggests intensive upward motion, leading to the reduction of effective potential energy and  
421 further develop of convective. Notably, the GTS12 radiosonde, launched from Wuhan, ceased data collection  
422 after the ascent phase, thus missing this crucial change. The descent phase of ADDRS demonstrates  
423 robust monitoring capabilities and holds significant implications, as it can timely captures environmental  
424 conditions favorable for convection onset and development, including wind patterns, effective potential energy,  
425 and humidity at downstream locations. These findings enable researchers to analyze changes in the upper-air  
426 field and the occurrence of catastrophic weather convective systems.

删除[CMA MOC luo]: of



427

428 **Figure 9. Comparison of ADDRS and GTS12 radiosonde T-logP at the Wuhan station: (a) GTS12 radiosonde; (b)**  
 429 **ascent phase of ADDRS radiosonde; (c) descent phase of ADDRS radiosonde.**

430 **5.2 Applications in numerical weather prediction (NWP)**

431 Unlike GTS12 radiosondes, the ADDRS radiosondes provide measurement data of both ascent and descent  
 432 phase, for numerical weather prediction (NWP), achieving a similar role to intensive sounding and providing  
 433 more continuous, direct stratospheric measurement data (Zhang, X et al., 2025; Zhang, X.P et al. 2023). The  
 434 Numerical Department of the China Meteorological Administration developed the key technology for ADDRS  
 435 assimilation in the CMA-MESO 3DVar (three-dimensional variational mesoscale) (Zhuang et al. 2019) and  
 436 CMA-GFS 4DVar systems (four-dimensional Variational Global Forecast System) (Wang, R. W et al., 2021).  
 437 To avoid the tangent linear and adjoint models, the four-dimensional ensemble forecast error is introduced into  
 438 the CMA global data assimilation system, and the Hybrid-4D<sub>En</sub>Var assimilation scheme is developed. The  
 439 batch cycling forecast experiments and typhoon forecast experiments are conducted and compared with the  
 440 4DVar scheme (Gong et al., 2019; Wang, F et al., 2024). Specifically, this includes observation operators that  
 441 consider drift positions and vertical spacing methods, such as selecting the nearest radiosonde data from the  
 442 model layer for assimilation. But the assimilation of drift-phase observations faces three primary challenges:  
 443 first, the large warm bias in daytime temperature measurements, which significantly impacts assimilation quality;  
 444 second, the high likelihood of correlated observation errors due to the very high horizontal resolution of the data  
 445 (~100 m along-track) compared to the model grid. Current operational systems do not account for these error  
 446 correlations, necessitating data thinning to improve assimilation effectiveness. Third, determining the optimal  
 447 data segmentation or "batching" strategy for the continuous trajectory. Treating the entire drift phase as a single,  
 448 vertical profile at an average location introduces significant representativeness error, as it ignores the sonde's  
 449 substantial horizontal displacement. We employed the CMA-MESO system to conduct a measurement data  
 450 assimilation in the ADDRS descent phase across six test stations in the middle and lower reaches of the Yangtze  
 451 River from July 1 to July 31, 2021. We set up the control test (CTL) as in the CMA-MESO system, and the  
 452 observed data included traditional sounding data, ground reports, aircraft reports, cloud-guided wind, radar  
 453 radial wind, GNSS occultation refractive index, and ground-based GNSS retrieval of the atmospheric whole-  
 454 layer precipitation water. ADDRS data assimilation was added to the control CTL in the Down test.

455 The impact of the ADDRS descent phase measurement data on the precipitation forecast at CMA-MESO at  
 456 03, 06, 09, 15, 18, and 21 UTC (termed the warm start times) was evaluated. Compared to the TS (Threat Score),  
 457 the ETS (Equitable Threat Score) imposes stricter penalty for false alarms and missed reports, making the

删除[CMA MOC luo]: measurement data

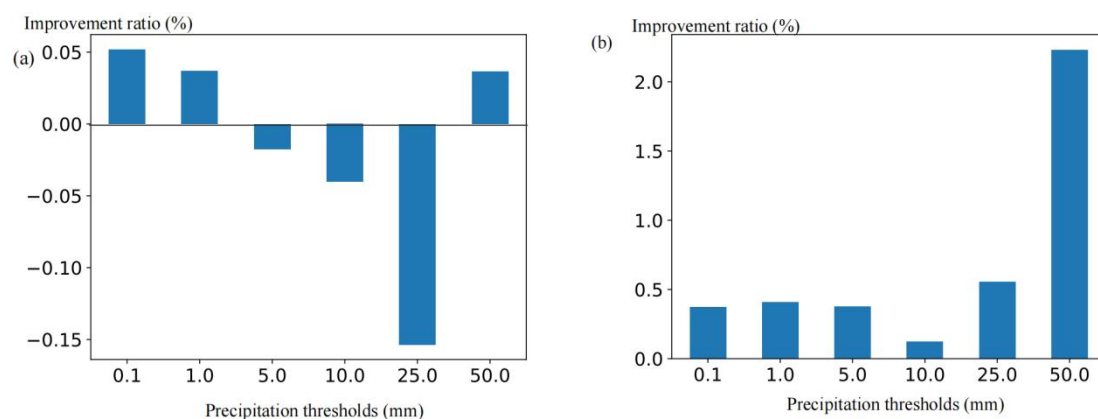
删除[云端]:

删除[CMA MOC luo]: .

458 scoring more equitable. The results of the one-month batch test indicate that assimilating ADDRS descent phase  
 459 data improves precipitation forecasting skills, especially for heavy precipitation above a certain magnitude. Fig.  
 460 10a and Fig. 10b illustrate the improvement rates in accumulated precipitation forecasting skills for the 0-12  
 461 hour and 12-24 hour periods from the warm start time. Positive values indicate that the precipitation forecasting  
 462 skills of the Down test are improved compared with those of the CTL test, while negative values indicate a  
 463 decrease in forecasting skills for the Down test. The ETS scores for precipitation forecasts in the 0-12 hour  
 464 range at thresholds of 0.1 mm, 1 mm, and 50 mm increased slightly, averaging about 0.04% (Fig. 10a). Due to  
 465 the timeliness required for forecasting, the 12-24 hour precipitation forecast is of particular interest to  
 466 forecasters. As illustrated in Fig. 10b, the Down test demonstrated enhanced ETS scores for precipitation  
 467 forecasts across all levels within the 12-24 hour range, with an average increase of 0.7% at the 50 mm  
 468 threshold and a notable 2.2% improvement specifically at this level. It is important to note that while these ETS  
 469 improvements are consistent and positive, they have not yet reached conventional levels of statistical  
 470 significance (e.g.,  $p < 0.05$ ) over the one-month test period, primarily due to the limited sample size of case  
 471 studies. This underscores the preliminary yet promising nature of these findings.

472 In addition, we utilized CMA-MESO V5.1 to conduct Observing System Simulation Experiments (OSSE)  
 473 under the ADDRS network nationwide. The results indicate that once the ADDRS network observation is  
 474 implemented, the national precipitation forecast skills of the CMA-MESO fast cycle assimilation forecast  
 475 system at warm startup time can improve by 2%-5%. The applications of ADDRS high-resolution data were  
 476 quantitatively evaluated using a numerical model (Wang, R. W et al., 2023). After the application of ADDRS  
 477 data in CMA-GFS 4DVar assimilation, the temperature analysis error at 06:00 and 18:00 was reduced by more  
 478 than 2% and the average prediction skill of the CMA-MESO accumulated precipitation results for the 12-36  
 479 hour period improved by 1% (Wang, J. C. et al., 2024).

删除[CMA MOC luo]: potential operational



480  
 481 **Figure 10. Improvement rates of cumulative precipitation thresholds (mm) predictions for 0-12 hours (a) and 12-24**  
 482 **hours (b) in the Down test compared to the control test.**

### 483 5.3 Applications in targeted observations

484 Targeted observations have sometimes been a frontier field in atmospheric science. They represent a  
 485 possible method to address the shortcomings of conventional observation systems in monitoring extreme  
 486 weather events. Furthermore, they sometimes enhance the initial field quality and forecast accuracy of  
 487 numerical models (Majumdar, 2016). With its capacity for “ADD” measurement, the ADDRS has the potential

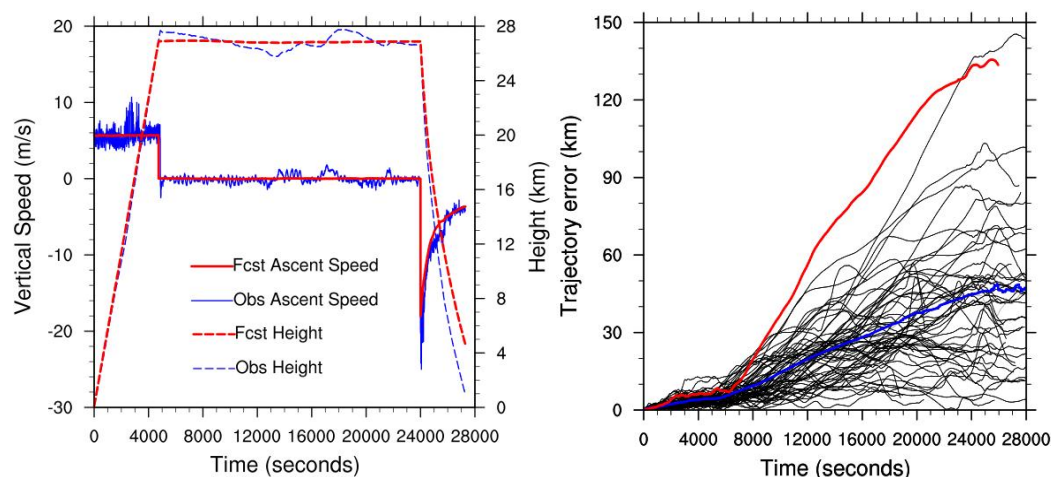
删除[CMA MOC luo]: one of  
 删除[CMA MOC luo]: research  
 删除[CMA MOC luo]: operatio  
 删除[CMA MOC luo]: .

488 to conduct targeted observations in uninhabited areas, rarely observed regions, and during specific extreme  
489 weather events. However, since the ADDRS lacks a steering system, accurate trajectory prediction is essential  
490 for utilizing the descent phase for vertical measurements in these locations. This requires careful consideration  
491 of appropriate drift height, launch time, and launch location, allowing the ADDRS sounding to be carried to the  
492 target observation area by the ambient wind field.

493 In this context, a trajectory prediction and selection method based on high-resolution numerical weather  
494 prediction technology has been proposed for ADDRS (Wang, J. C et al., 2021). Additionally, Majumdar (2016)  
495 highlights that advancements in numerical weather prediction (NWP) systems—such as improved data  
496 assimilation techniques and enhanced model resolution—have reduced the marginal contributions of individual  
497 observing systems. Furthermore, the evaluation of targeted observations is constrained by factors including  
498 flow-dependent conditions, limited sample sizes, and inconsistencies in verification metrics. Therefore, cost-  
499 effective strategies for targeted observations necessitate exploration through multi-agency coordinated  
500 observing system experiments, such as FSO studies (Magnusson et al., 2025).

### 501 5.3.1 Trajectory prediction method and software system

502 The issues of low temporal resolution and prediction accuracy associated with the linear extrapolation  
503 method used in balloon trajectory prediction (Brown et al., 2024). The balloon trajectory equation is directly  
504 embedded into a high-resolution numerical weather model system that utilizes a model atmospheric  
505 environment with high temporal resolution (1-10 seconds) and high spatial resolution (1-3 km). This approach  
506 enables precise simulation of vertical velocity during the ADDRS descent phase (Fig. 11a), enhancing the  
507 accuracy of ADDRS trajectory prediction and the simulation of descent velocity. The average prediction error  
508 for a 6-hour trajectory is less than 40 km (Fig. 11b).



509  
510 **Figure 11. (a) Comparison of simulated (red line) and observed (blue line) vertical speeds of ADDRS radiosonde data**  
511 **during the descent phase at the Anqing station at 11:17 on June 20, 2018; (b) Deviations of 63 pairs of simulated**  
512 **ADDRS trajectories versus observed trajectories (black line), with the average deviation indicated by the blue line**  
513 **and the largest forecast deviation shown by the red line.**

### 514 5.3.2 Trajectory selection method based on the collection idea

515 To observe the ADDRS in the target observation area, we proposed a method of elevation selection based  
516 on ensemble forecasting, considering the characteristics of the atmospheric wind field as it varies with altitude.

517 The main idea of this method is to predict the trajectories of all ADDRS stations at different drifting heights and  
518 select the heights closest to the target observation area. The details are as follows:

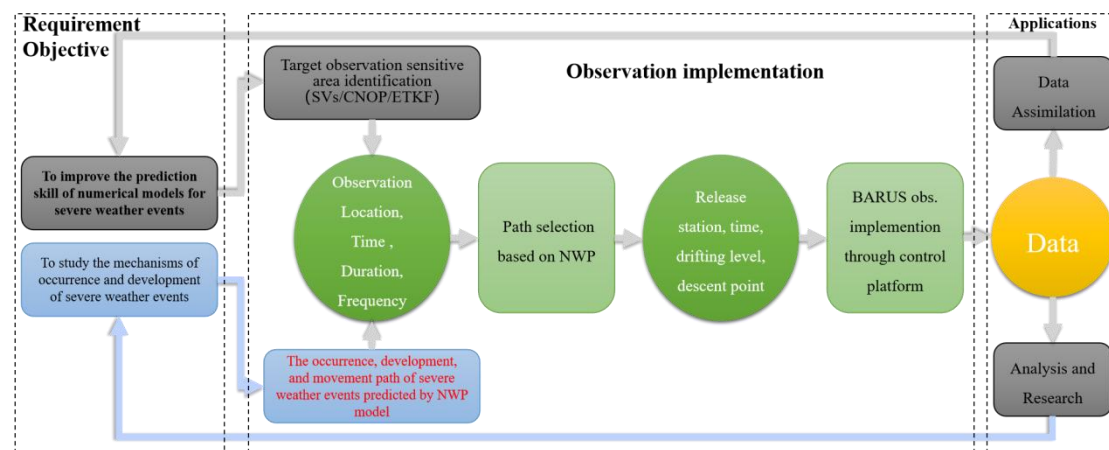
- 519 1. Identify the positions and launch time: Given the positions  $S_m(x_m, y_m, z_m)$  of  $M$  ADDRS launch stations and  
520 the launch time  $t_r$ .
- 521 2. Select safe drift heights: Choose  $N$  safe drift heights  $h_1, h_2, \dots, h_n$ , that comply with civil aviation safety  
522 regulations as flat drift heights.
- 523 3. Trajectory prediction: Utilize the trajectory prediction system to predict the ADDRS trajectories under the  
524 above conditions within 12 hours, resulting in  $T_{nm}(x, y, z, t)$  for  $N$  trajectories at each of the  $M$  launch  
525 stations.
- 526 4. Calculate closest trajectory: From the  $M \times N$  trajectories obtained in step 3, calculate the trajectory closest  
527 to the target observation point. When the distance is less than the predetermined standard distance  $L_C$  that  
528 can meet the requirements, the releasing ADDRS station and the drifting height  $H_s$  are selected, and the  
529 time nearest to the target area is taken as the descent time  $t_s$ . If no suitable drift height meets the conditions,  
530 the trajectory selection fails.
- 531 5. Implement target observation: Input the information regarding the ADDRS balloon launch station, drift  
532 height, and descent time determined in step 4 into the ADDRS operation command system to execute the  
533 target observation.

### 534 5.3.3 Targeted observations experiment of Typhoon

535 The ADDRS research team proposed a 'full chain' implementation for target observation using ADDRS  
536 (Fig. 12). This implementation plan, designed to provide technical support for ADDRS applications in disaster  
537 weather monitoring, forecasting, and mechanism research, encompasses three primary phases. Initially, the  
538 requirements for target observation are established. These requirements fall into two categories: one focusing on  
539 specific disaster weather events and the other on sensitive areas to improve future numerical prediction skills.  
540 The target observation area is then determined based on the type of demand. For the first category, the specific  
541 location of anticipated disaster weather is identified through numerical prediction results. For the second  
542 category, the target observation location is determined using CMA-GFS singular vector technology.

543 Subsequently, the trajectory selection system is invoked to ascertain the ADDRS launch station, drift  
544 height, launch and subsequent descent phases time, and other relevant information. This information is then  
545 transmitted to the operation command system of ADDRS to guide the stations in implementing ADDRS  
546 measurements. Ultimately, the ADDRS target observation data is distributed to users for application and  
547 evaluation.

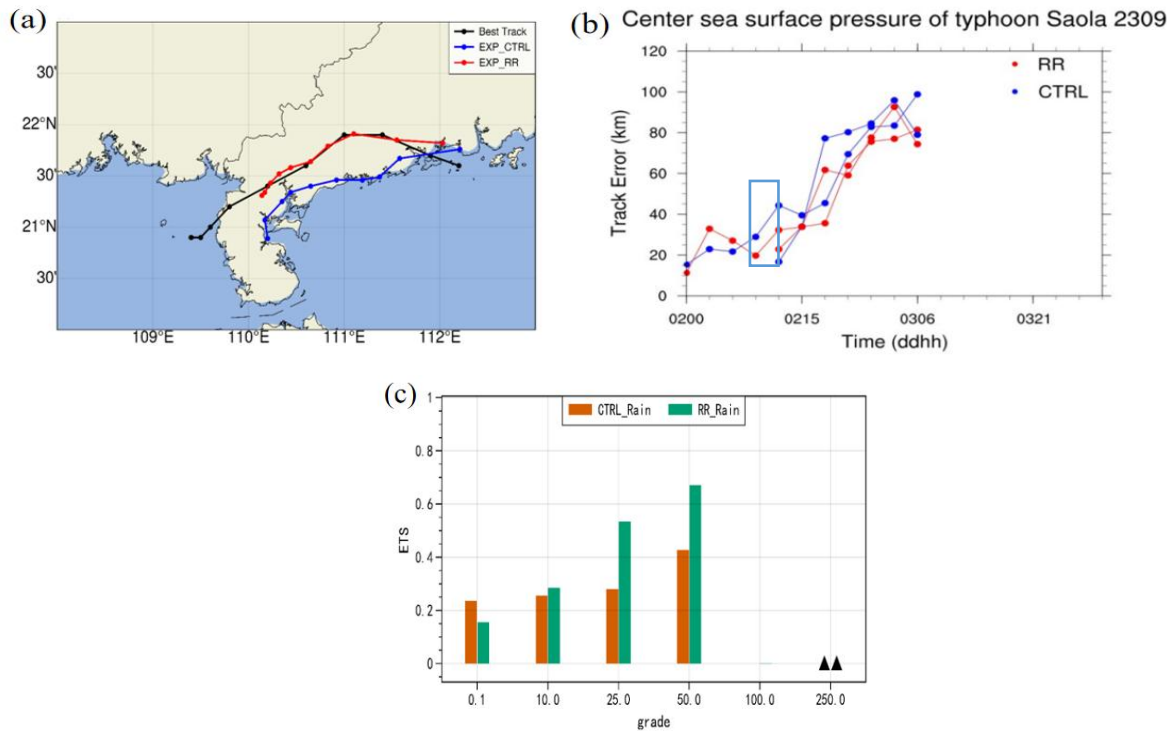
| 删除[CMA MOC luo]: discharge radiosonde observations



548  
549 **Figure 12. Technical route for targeted observations of typhoons and other severe weather using ADDRS and CMA-**  
550 **MESO models.**

551 According to the implementation plan for ADDRS target observation (Zhang et al., 2021; Liu, L. H et al.,  
552 2022), we made a preliminary attempt to conduct a target observation experiment on Typhoon 2309 'SAOLA'  
553 (Lau et al., 2024) formed at 00 UTC on August 28, 2023. By 00 UTC on September 1, it was expected that  
554 'SAOLA' would **make landfall** near Guangdong on September 2nd. Therefore forecasters sought profiles of the  
555 inner structure of Typhoon 'SAOLA'. Note also the importance of the steering flow and use of satellite data to  
556 analyse the wider environment of tropical storms (Magnusson et al, 2025). Using the typhoon trajectory  
557 predicted by CMA-GFS, we pinpointed the typhoon's position for 12:00 PM on September 2 post-landfall. The  
558 ADDRS trajectory selection system was then engaged to ascertain the balloon launch station and drift height  
559 that could reach or come closest to the typhoon area, ranging from the minimum navigation safety height of 21  
560 km to 29 km. We set ten different drift levels at 1 km intervals, with trajectory predictions and simulations  
561 conducted from four radiosonde observations stations in Guangdong. Yangjiang radiosonde observations station  
562 in Guangdong was ultimately chosen for the launch, scheduled for 06:00 on September 2, 2023, with a drift  
563 level of 25 km.

564 We calculated the required hydrogen capacity for the dual-mode balloon, and the 'ADD' subsystem was  
565 prepared to be deployed by radiosonde observations station personnel. When the radiosonde reached the core  
566 area of 'SAOLA' the radiosonde dispatched commands to the 'SAOLA' controller via control command  
567 transmission equipment, successfully observing the descent phase 80 km from the center of Typhoon 'SAOLA'  
568 The obtained ADDRS data was subsequently assimilated into the CMA\_MESO 3DVar system. Test results  
569 indicated that after assimilating the data from the ADDRS descent phase, the forecast error for the typhoon  
570 trajectory reported since 06:00 on September 2, 2023, was reduced. Specifically, the typhoon trajectory error at  
571 02:18 was reduced from 62.7 km to 35 km in the control test, marking an improvement of 44.18%. Additionally,  
572 precipitation forecasting techniques exhibited improvements: from 0.25 to 0.30 in the 10 mm scale, from 0.30 to  
573 0.55 in the 25 mm scale, and from 0.45 to 0.70 in the 50 mm scale. These results effectively demonstrate the  
574 potential of ADDRS in target observation and numerical assimilation applications (Fig. 13). It is worth noting  
575 that the initial use of ADDRS for target observation served as a foundational attempt, paving the way for future  
576 ADDRS operations and maximizing its utility (Wen., et al., 2024).



577

578

579 **Figure 13. 2023-09-02 UTC 00-12h: (a) Control test (blue), ADDRS data assimilation impact test (red), and optimal**  
 580 **trajectory of Typhoon 'Saola' (black); (b) Comparison of sea level pressure at the central point of Typhoon 'Saola'**  
 581 **between the control test (blue) and the ADDRS data assimilation impact test (red); (c) ETS scores for 0-24 hours of**  
 582 **precipitation forecast from control trials (orange) and ADDRS data assimilation impact trials (green).**

583 **6. Summary**

584 ADDRS represents a possible next-generation approach for upper air sounding, adding substantial  
 585 flexibility compared to currently operational sounding systems. We developed a multi-station real-time  
 586 reception system utilizing 'Internet cloud + Instruments terminal' technology. Additionally, uplink commands  
 587 can be sent from the ground to facilitate descent measurements in designated areas and targeted observations in  
 588 weather-sensitive regions. Following over five years of extensive research and numerous field tests, the  
 589 instruments, software, and operation guidelines of the system have achieved a refined level of maturity. Starting  
 590 January 1, 2024, ADDRS already undergo operation experiments at four radiosonde observations stations in  
 591 Guangdong, China. Since July 2024, a planned trial at 127 CMA radiosonde observation stations aims to  
 592 achieve full operation capability by 2026. The positive impact of ADDRS data assimilation demonstrated here,  
 593 even if not yet statistically significant over a one-month sample, has shown considerable applicable promise.  
 594 ADDRS is a situational profiling technique that offers cost-effective upper-air measurements, making it suitable  
 595 for widespread application in WMO's pre-operational sounding (e.g., RA II-18-I-DP-2). However, challenges  
 596 remain, such as improving the drift success rate, enhancing relevant technologies, and fully leveraging the  
 597 potential of continuous measurement data during the drift phase.

599 **Data Availability Statement:** The ADDRS research team is currently building a new data-sharing platform  
 600 (<https://www.r7tec.com/html/report/20040875-1.htm>), which will be available for scientific sharing to registered

删除[CMA MOC luo]: surpassing the 20th century operational method.

删除[CMA MOC luo]: al

删除[CMA MOC luo]: al

删除[CMA MOC luo]: operational

删除[CMA MOC luo]: s

删除[CMA MOC luo]: al

删除[CMA MOC luo]: across all CMA radiosonde observations stations

删除[CMA MOC luo]: operational

删除[CMA MOC luo]: We are confident that statistically significant improvements in precipitation forecast skills will be achieved as the data records lengthen and the number of case studies, particularly for extreme precipitation events, increases in the future.

删除[CMA MOC luo]: s

删除[CMA MOC luo]: With the constant development of ADDRS and the continuous deepening of the measurement data, ADDRS will become a development direction for future operational upper-air observation applications and scientific research.

删除[CMA MOC luo]: **Acknowledgments:**

The authors are thankful to theEditor and all anonymous reviewers for their help in im-proving this manuscript.

601 users starting in December [2025](#). More data acquisition requires formal request to the corresponding author <  
602 gqyaoc@cma.gov.cn> for restricted availability.

603 **Team list:** Xiaozhong Cao<sup>\*1</sup>, Qiyun Guo<sup>2,3,4</sup>, Haowen Luo<sup>2,3,4</sup>, [Jincheng Wang<sup>5</sup>](#), Rongkang Yang<sup>2,3,4</sup>, Die Xiao<sup>6</sup>,  
604 [Yinfeng Liu<sup>7</sup>](#), Zhongliang Sun<sup>8</sup>, Shijun Liu<sup>9</sup>, Sijie Chen<sup>10</sup>, Anfan Huang<sup>2,3,4</sup>, [Guo Jianping<sup>11</sup>](#), Peng Zhang<sup>\*2,3,4</sup>

605 **Author contribution:** XC, PZ, [conceptualization and methodology](#); QG and HL designed the experiments and  
606 [writing-original draft, supervision](#); JW, DX, JD, ZS, SL carried out the experiments; [HL, QG, JW, RY](#), analyzed  
607 the experimental results; [HL, QG, GJ, SC, AH](#) revised the paper and participated in the discussion. **Competing**  
608 **interests:** The contact author has declared that none of the authors has any competing interests.

609 **Disclaimer:** Copernicus Publications remains neutral with regard to jurisdictional claims made in the text,  
610 published maps, institutional affiliations, or any other geographical representation in this paper. While  
611 Copernicus Publications makes every effort to include appropriate place names, the final responsibility lies with  
612 the authors.

613 **Acknowledgments:** [The authors are thankful to the editor and all anonymous reviewers for their help in im-](#)  
614 [proving this manuscript.](#)

615 **Financial support:** This research has been supported by the National Natural Science Foundation of China  
616 (grant no. U2442214); the National Key Research and Development Program (grant no. 2018YFC1506200); the  
617 Innovation Team of the China Meteorological Administration (grant no. CMA2023QN11).

618

设置格式[CMA MOC luo]: 字体: 加粗

设置格式[CMA MOC luo]: 上标

设置格式[CMA MOC luo]: 上标

设置格式[CMA MOC luo]: 上标

删除[CMA MOC luo]: 2

设置格式[CMA MOC luo]: 字体: 非加粗, 上标

删除[CMA MOC luo]: 2

删除[CMA MOC luo]: Guo Jianping3, Jincheng Wang4,

删除[CMA MOC luo]: 5

设置格式[CMA MOC luo]: 上标

删除[CMA MOC luo]: Jianping

删除[CMA MOC luo]: D

删除[CMA MOC luo]: 6

设置格式[CMA MOC luo]: 上标

删除[CMA MOC luo]: 7

设置格式[CMA MOC luo]: 上标

删除[CMA MOC luo]: 8

设置格式[CMA MOC luo]: 上标

删除[CMA MOC luo]: 9

设置格式[CMA MOC luo]: 上标

删除[CMA MOC luo]: 2

设置格式[CMA MOC luo]: 上标

设置格式[云端]: 上标

删除[CMA MOC luo]: 2

删除[CMA MOC luo]:

设置格式[CMA MOC luo]: 字体: 加粗

删除[CMA MOC luo]: s.

设置格式[CMA MOC luo]: 字体: 加粗

删除[CMA MOC luo]:

删除[CMA MOC luo]: wrote the paper

删除[CMA MOC luo]: JW

删除[CMA MOC luo]: .

删除[CMA MOC luo]:

设置格式[CMA MOC luo]: 字体: 加粗

619 **References**

620 Anand, D., Kumar, B. S., and Ojha, D.: TIFR Zero-Pressure balloon program crosses a milestone, *Current*  
621 *Science*, 2021, 120, 1672-1678, <https://doi.org/10.18520/cs/v120/i11/1672-1678>, 2021.

622 Bauer, P., Thorpe, A., Brunet, G.: The quiet revolution of numerical weather prediction, *Nature*, 2015, 525, 47–  
623 55, <https://doi.org/10.1038/nature14956>, 2015.

624 [Bauer, P., G. Radnóti., S. Healy., C. Cardinali.: GNSS Radio Occultation Constellation Observing System](#)  
625 [Experiments, \*Mon. Wea. Rev.\*, 142, 555–572, <https://doi.org/10.1175/MWR-D-13-00130.1>, 2014.](#)

626 Bormann, N., Lawrence, H., Farnan, J.: Global observing system experiments in the ECMWF assimilation  
627 system, *ECMWF Technical Memorandum*, 2019, 839, 24, <https://doi.org/10.21957/sr184iyz>, 2019.

628 Bauer, P., G. Radnóti., S. Healy., C. Cardinali.: GNSS Radio Occultation Constellation Observing System  
629 Experiments, *Mon. Wea. Rev.*, 142, 555–572, <https://doi.org/10.1175/MWR-D-13-00130.1>, 2014.

630 Brown, D., Linz, M. & Leidich, J.: Seasonal and geographic viability of high altitude balloon navigation, *Sci*  
631 *Rep.*, 14, 21861 (2024), <https://doi.org/10.1038/s41598-024-71445-9>, 2024.

632 [Cao, X. Z., Xia, Y. C., Luo, H. W., Liu, L. H., Liu, Y. F., Liu, Z. Y., Li, X., Guo, R., and Guo, Q. Y.: Technical](#)  
633 [development and prospect of meteorological sounding measurement, \*J. Adv. Meteorol. Sci. Technol.\*, 12,](#)  
634 [27-36, <https://doi.org/10.3969/j.issn.2095-1973.2022.05.005>, 2022. \(in Chinese\)](#)

635 [Cao, X. Z., Guo, Q. Y., Yang, R. K.: Research of rising and falling twice sounding based on long-time interval](#)  
636 [of flat-floating, \*Chinese Journal of Scientific Instrument.\*, 40\(2\): 198-204.](#)  
637 <http://yqyb.etmchina.com/yqyb/article/abstract/20190223?st=search>, 2019. (in Chinese)

638 [Cohn, S., Hock, T., Cocquerez, P., & Cole, H.: Driftsondes: providing in situ long-duration dropsonde](#)  
639 [observations over remote regions, \*Amer. Meteor. Soc.\*, 94, 1661–1674, \[12-00075.1\]\(https://doi.org/10.1175/BAMS-D-</a></a><br/>640 <a href=\), 2013.](#)

641 [DuBois, J. L., Multhaupt, R. P., and Ziegler, C. A.: Invention and Development of the Radiosonde with a Catalog](#)  
642 [of Upper-Atmospheric Telemetering Probes in the National Museum of American History, Smithsonian](#)  
643 [Institution, \*Smithsonian Studies in History and Technology\*, 2002, 53, 1-78,](#)  
644 <https://doi.org/10.5479/si.00810258.53.1>, 2002.

645 Fujiwara, M., Sun, B., Reale, A., Cimini, D., Larosa, S., Borg, L., von Rohden, C., Sommer, M., Dirksen, R.,  
646 Maturilli, M., Vömel, H., Kivi, R., Ingleby, B., Kramer, R. J., Demoz, B., Madonna, F., Carminati, F.,  
647 Lewis, O., Candy, B., Thomas, C., Edwards, D., Noersomadi, Shimizu, K., and Thorne, P.: Justification for  
648 high-ascent attainment for balloon radiosonde observations at GRUAN and other sites, *Atmos. Meas. Tech.*,  
649 2025, 18, 2919–2955, <https://doi.org/10.5194/amt-18-2919-2025>, 2025.

650 Gallice, A., Wienhold, F. G., Hoyle, C. R., Immler, F., and Peter, T.: Modeling the ascent of sounding balloons:  
651 derivation of the vertical air motion, *Atmos. Meas. Tech.*, 2011, 4, 2235-2253, [https://doi.org/10.5194/amt-](https://doi.org/10.5194/amt-4-2235-2011)  
652 [4-2235-2011](#), 2011.

653 Gong, N., Liu, Y. F., Ren, J., Wu, Q., and Hu, H. L.: A Novel Adaptive Resource Allocation Framework for  
654 Sounding Networks, 2021 the 11th International Workshop on Computer Science and Engineering (WCSE  
655 2021) , 276-283, <https://doi.org/10.18178/wcse.2021.06.040>, 2021.

656 [Gong, J. D., Liu, Y. Z., Zhang, L.: A study of simplification and linearization of the NSAS deep convection](#)  
657 [cumulus parameterization scheme for 4D-Var, \*Acta Meteorologica Sinica.\*, 77, 595-616,](#)  
658 <https://doi.org/10.11676/qxxb2019.048>, 2019. (in Chinese)

删除[CMA MOC luo]: REFERENCES

设置格式[CMA MOC luo]: 字体: 加粗

删除[CMA MOC luo]: doi:

删除[CMA MOC luo]: doi:

删除[CMA MOC luo]: pp.

删除[CMA MOC luo]: doi:

删除[CMA MOC luo]: 2014,

删除[CMA MOC luo]: doi:

删除[CMA MOC luo]:

删除[CMA MOC luo]: .

删除[CMA MOC luo]: doi:

删除[CMA MOC luo]: doi:

删除[CMA MOC luo]: Cao, X. Z., Xia, Y. C., Luo, H. W.,  
Liu, L. H., Liu, Y. F., Liu, Z. Y., Li, X., Guo, R., and Guo, Q.  
Y.: Technical development and prospect of meteorological  
sounding measurement, *J. Adv. Meteorol. Sci. Technol.*, 12,  
27-36, 2022, doi:[https://doi.org/10.3969/j.issn.2095-](https://doi.org/10.3969/j.issn.2095-1973.2022.05.005)  
1973.2022.05.005.(in Chinese)

Cao, X. Z., Guo, Q. Y., Yang, R. K.: Research of rising and  
falling twice sounding based on long-time interval of flat-  
floating, *Chinese Journal of Scientific Instrument*, 2019,40(2):  
198-204.  
<http://yqyb.etmchina.com/yqyb/article/abstract/20190223?st=search>  
(in Chinese)

删除[CMA MOC luo]: doi:

删除[CMA MOC luo]: s

删除[CMA MOC luo]: doi:

删除[CMA MOC luo]: doi:

删除[CMA MOC luo]: doi:

659 Guo, Q. Y., Yang, J. C., Yang, R. K., Qian, Y., and Cao, X. Z.: Evaluation of wind performance of domestic  
660 Beidou dropsonde of ball-loading, *J. Nanjing Univ. Inf. Eng.: Nat. Sci. Ed.*, 10,  
661 12, <https://doi.org/10.13878/j.cnki.jnuist.2018.05.014>, 2018. (in Chinese)  
662 Haig, T. O., and V. E. Lally: Meteorological Sounding Systems, *Bull. Amer. Meteor. Soc.*, 39, 401–  
663 409, <https://doi.org/10.1175/1520-0477-39.8.401>, 1958.  
664 He, Y., Zhu, X., Sheng, Z., and He, M.: Identification of stratospheric disturbance information in China based  
665 on the round-trip intelligent sounding system, *Atmos. Chem. Phys.*, 2024, 24, 3839–3856,  
666 <https://doi.org/10.5194/acp-24-3839-2024>, 2024.  
667 Hersbach, H., Bell, B., Berrisford, P., Hirahara, S., Horányi, A., Muñoz - Sabater, J., Nicolas, J., Peubey, C.,  
668 Radu, R., Schepers, D., Simmons, A., Soci, C., Abdalla, S., Abellan, X., Balsamo, G., Bechtold, P., Biavati,  
669 G., Bidlot, J., Bonavita, M., De Chiara, G., Dahlgren, P., Dee, D., Diamantakis, M., Dragani, R., Flemming,  
670 J., Forbes, R., Fuentes, M., Geer, A., Haimberger, L., Healy, S., Hogan, R. J., Hólm, É., Janisková, M.,  
671 Keeley, S., Laloyaux, P., Lopez, P., Lupu, C., Radnoti, G., de Rosnay, P., Rozum, I., Vamborg, F.,  
672 Villaume, S., Thépaut, J. - N.: The ERA5 global reanalysis, *Q. J. R. Meteorolog.*  
673 *Soc.*, <https://doi.org/10.1002/qj.3803>, 2020.  
674 Ingleby, B., Pauley, P., Kats, A., Ator, J., and Weedon, R.: Progress toward high-resolution, real-time  
675 radiosonde reports, *Bull. Amer. Meteor. Soc.*, 97, 2149–2161, [00169.1](https://doi.org/10.1175/BAMS-D-15-</a></u><br/>
676 <u><a href=), 2016a.  
677 Ingleby, B., Rodwell, M., Isaksen, L.: Global radiosonde network under pressure, ECMWF Newsletter No. 149  
678 – Autumn 2016., pp. 25 - 30, [https://www.ecmwf.int/sites/default/files/elibrary/2016/18147-global-](https://www.ecmwf.int/sites/default/files/elibrary/2016/18147-global-radiosonde-network-under-pressure.pdf)  
679 [radiosonde-network-under-pressure.pdf](https://www.ecmwf.int/sites/default/files/elibrary/2016/18147-global-radiosonde-network-under-pressure.pdf), 2016b.  
680 Ingleby, B.: An assessment of different radiosonde types 2015/2016. ECMWF Technical Memorandum No. 807,  
681 69 pp. <https://doi.org/10.21957/0nje0wpsa>, 2017.  
682 Ingleby, B., Motl, M., Marlton, G., Edwards, D., Sommer, M., von Rohden, C., Vömel, H., and Jauhiainen, H.:  
683 On the quality of RS41 radiosonde descent data, *Atmos. Meas. Tech.*, 2022, 15, 165–  
684 183, <https://doi.org/10.5194/amt-15-165-2022>, 2022.  
685 Johnson, A., Wang, X., Hutchinson, T., and Creus-Costa, J.: Impact of WindBorne observation assimilation on  
686 prediction of a TPV merger case from THINICE, *J. Geophys. Res. Atmospheres.*, 129,  
687 e2024JD041395, <https://doi.org/10.1029/2024JD041395>, 2024.  
688 Lau, D.S., Chan, W.S., Wong, Y.C., Lam, C.C., Chan, P.W.: Hindcast Insights from Storm Surge Forecasting of  
689 Super Typhoon Saola (2309) in Hong Kong with the Sea, Lake and Overland Surges from Hurricanes  
690 Model, *Atmos.*, 15, 17, <https://doi.org/10.3390/atmos15010017>, 2024.  
691 Liu, S. J., Yang, R. K., Cao, X. Z., Guo, Q. Y., Cheng, K. Q., Kan, Z. P., and Wang, J. C.: Analysis and  
692 Numerical Experiment of the Horizontal Drift Round-trip Sounding Balloon's Dynamic and Thermal  
693 Process in the Adjacent Space, *Chin. J. Atmos. Sci.*, 46, 788–804, [https://doi.org/10.3878/j.issn.1006-](https://doi.org/10.3878/j.issn.1006-9895.2110.20252)  
694 [9895.2110.20252](https://doi.org/10.3878/j.issn.1006-9895.2110.20252), 2022. (in Chinese)  
695 Liu, Y. F., Zhou, Y. Y., Du, J. P., Liu, D., Ren, J., Chen, Y. H., Zhang, F., and Chen, J. P.: RTP-GRU:  
696 Radiosonde Trajectory Prediction Model Based on GRU, in *Proceedings.*, 24, [https://doi.org/10.1007/978-](https://doi.org/10.1007/978-981-15-8462-6_61)  
697 [981-15-8462-6\\_61](https://doi.org/10.1007/978-981-15-8462-6_61), 2021.

删除[CMA MOC luo]: doi:  
删除[CMA MOC luo]: Gong, J. D., Liu, Y. Z., Zhang, L.: A study of simplification and linearization of the NSAS deep convection cumulus parameterization scheme for 4D-Var, *Acta Meteorologica Sinica*, 2019, 77, 595-616, doi:<https://doi.org/10.11676/qxxb2019.048>.(in Chinese)  
删除[CMA MOC luo]: , 1958  
删除[CMA MOC luo]: .  
删除[CMA MOC luo]: doi:  
删除[CMA MOC luo]: doi:  
删除[CMA MOC luo]: doi:  
删除[CMA MOC luo]: Ingleby, B., and Coauthors, 2016: Progress toward High-Resolution, Real-Time Radiosonde Reports. *Bull. Amer. Meteor. Soc.*, 97, 2149–2161, doi:<https://doi.org/10.1175/BAMS-D-15-00169.1>.  
删除[CMA MOC luo]:  
删除[CMA MOC luo]: doi:  
删除[CMA MOC luo]: Ingleby, B., 2021: Use of radiosonde descent data from ships, ECMWF Newsletter, Page 5 doi:[https://www.ecmwf.int/sites/default/files/elibrary/102021/20225-newsletter-no-169-autumn-2021\\_1.pdf](https://www.ecmwf.int/sites/default/files/elibrary/102021/20225-newsletter-no-169-autumn-2021_1.pdf).  
删除[CMA MOC luo]: doi:  
删除[CMA MOC luo]: 2024,  
删除[CMA MOC luo]: doi:  
删除[CMA MOC luo]: Jensen, M. P., Holdridge, D. J., Survo, P., Lehtinen, R., Baxter, S., Toto, T., and Johnson, K. L.: Comparison of Vaisala radiosondes RS41 and RS92 at the ARM Southern Great Plains site, *Atmos. Meas. Tech.*, 2016, 9, 3115–3129, doi:<https://doi.org/10.5194/amt-9-3115-2016>.  
删除[CMA MOC luo]: 2022,  
删除[CMA MOC luo]: doi:  
删除[CMA MOC luo]: 2021,

698 [Liu, L. H.; Han, Y.; Xia, Y. C.; Guo, Q. Y.; Gao, W.; Guo, J. P.: Investigation of Atmospheric Dynamic and](#)  
699 [Thermodynamic Structures of Typhoon Sinlaku \(2020\) from High-Resolution Dropsonde and Two-Way](#)  
700 [Rawinsonde Measurements, Remote Sens., 14, 2704, <https://doi.org/10.3390/rs14112704>, 2022.](#) 删除[CMA MOC luo]: Liu, B., Guo, J., Gong, W., Zhang (...)

701 [Magnusson, L., Majumdar, S.J., Dahoui, M.L., Bormann, N., Bonavita, M., Browne, P.A., Brown, A.R., De](#)  
702 [Chiara, G., Duncan, D.I., English, S., Geer, A.J., Healy, S., Ingleby, B., McNally, A.P., Pappenberger, F.,](#)  
703 [Prates, F., Rabier, F., de Rosnay, P., Rennie, M.P., Warrick, F.: The role of observations in ECMWF](#)  
704 [tropical cyclone initialisation and forecasting, Q. J. R. Meteorolog. Soc., 151\(768\),](#)  
705 [e4924, <https://doi.org/10.1002/qj.4924>, 2025.](#) 删除[CMA MOC luo]: .  
706 [Magnusson, L., Majumdar, S.J.: A review of targeted observations, Bull. Am. Meteorol. Soc., 97, 2287-](#)  
707 [2303, <https://doi.org/10.1175/BAMS-D-14-00259.1>, 2016.](#) 删除[CMA MOC luo]: 2022  
708 [Marlton GJ, Harrison RG, Nicoll KA, Williams PD.: A balloon-borne accelerometer technique for measuring](#)  
709 [atmospheric turbulence, Rev. Sci. Instrum., 86, 016109, <https://doi.org/10.1063/1.4905529>, 2015.](#) 删除[CMA MOC luo]: doi:  
710 [Pauley, P.M., and Ingleby, B.: Assimilation of in-situ observations, In S.K. Park & L. Xu \(Eds.\), Data](#)  
711 [Assimilation for Atmospheric, Oceanic and Hydrologic Applications \(Vol. IV\)\(pp. 293–371\). Springer,](#)  
712 [Cham, \[https://doi.org/10.1007/978-3-030-77722-7\\\_12\]\(https://doi.org/10.1007/978-3-030-77722-7\_12\), 2022.](#) 删除[CMA MOC luo]: Lau, D.S., Chan, W.S., Wong, Y.C (...)

713 [Pettifer, R. E.: From Observations to Forecasts - Part 2. The development of in situ upper air measurements,](#)  
714 [Weather, 2009, 64, <https://doi.org/10.1002/wea.484>.](#) 删除[CMA MOC luo]: 2016,  
715 [Raman, M. R., Ratnam, M. V., Rajeevan, M., Rao, V. V. M. J., Rao, S. V. B.: Intriguing Aspects of the](#)  
716 [Monsoon Low-Level Jet over Peninsular India Revealed by High-Resolution GPS Radiosonde](#)  
717 [measurements, J. Atmos. Sci., 68, 1413–1423, <https://doi.org/10.1175/2011JAS3611.1>, 2011.](#) 删除[CMA MOC luo]: doi:  
718 [Ratnam, M. V., Pravalika, N., Babu, S. R., Basha, G., Pramitha, M., Murthy, B. V. K.: Assessment of GPS](#)  
719 [radiosonde descent data, Atmos. Meas. Tech., 7\(4\), <https://doi.org/10.5194/amt-7-1011-2014>, 2014.](#) 删除[CMA MOC luo]: 2011,  
720 [Roth, S., and Yoder, C. D.: Balloon missions soar to new heights, Aerospace America., 60\(11\), 35-35.](#)  
721  [<https://aerospaceamerica.aiaa.org/year-in-review/balloon-missions-soar-to-new-heights>, 2022.](#) 删除[CMA MOC luo]: doi:  
722 [Seidel, D. J., Berger, F. H., Diamond, H. J., Dykema, J., Goodrich, D., Immler, F., Murray, W., Peterson, T.,](#)  
723 [Sisterson, D., Sommer, M., Thorne, P., Vomel, H., & Wang, J.: Reference Upper-Air Observations for](#)  
724 [Climate: Rationale, Progress, and Plans, Bulletin of the American Meteorological Society., 90\(3\), 361-](#)  
725 [369, <https://doi.org/10.1175/2008BAMS2540.1>, 2009.](#) 删除[CMA MOC luo]: &  
726 [Shen, Z. P., Pan, X. Z., and Yi, Y. L.: Preparation and properties of modified nano-clay/natural latex composites,](#)  
727 [J. Rubber Ind., 67, 4, <https://doi.org/10.12136/j.issn.1000-890X.2020.08.0580>, \(in Chinese\)](#) 删除[CMA MOC luo]: .  
728 [Vernier, J. - P., Fairlie, T. D., Deshler, T., Ratnam, M. V., Gadhavi, H., Kumar, B. S., Natarajan, M., Pandit, A.](#)  
729 [K., Raj, S. T. A., Kumar, A. H., Jayaraman, A., Singh, A. K., Rastogi, N., Sinha, P. R., Kumar, S., Tiwari,](#)  
730 [S., Wegner, T., Baker, N., Vignelles, D., Stenichikov, G., Shevchenko, I., Smith, J., Bedka, K., Kesarkar, A.,](#)  
731 [Singh, V., Bhate, J., Ravikiran, V., Rao, M. D., Ravindrababu, S., Patel, A., Vernier, H., Wienhold, F. G.,](#)  
732 [Liu, H., Knepp, T. N., Thomason, L., Crawford, J., Ziemba, L., Moore, J., Crumeeyrolle, S., Williamson,](#)  
733 [M., Berthet, G., Jégou, F., Renard, J. B.: BATAL: The Balloon Measurement Campaigns of the Asian](#)  
734 [Tropopause Aerosol Layer, Bull. Am. Meteorol. Soc., 99, 955–973, \[https://doi.org/10.1175/BAMS-D-17-\]\(https://doi.org/10.1175/BAMS-D-17-0014.1\)](#)  
735 [-0014.1, 2018.](#) 删除[CMA MOC luo]: 2022,  
736 [Vernier, H., Rastogi, N., Liu, H., Pandit, A. K., Bedka, K., Patel, A., Ratnam, M. V., Kumar, B. S., Zhang, B.,](#)  
737 [Gadhavi, H., Wienhold, F., Berthet, G., and Vernier, J.-P.: Exploring the inorganic composition of the](#) 删除[CMA MOC luo]: doi:  
738 删除[CMA MOC luo]: 2020,  
739 删除[CMA MOC luo]: doi:  
740 删除[CMA MOC luo]: 2018,  
741 删除[CMA MOC luo]: doi:

738 Asian Tropopause Aerosol Layer using medium-duration balloon flights, *Atmos. Chem. Phys.*, 22, 12675–  
739 12694, <https://doi.org/10.5194/acp-22-12675-2022>, 2022.

740 [Wang, D., Wang, J. C., Tian, W. H., Guo, Q. Y.: Quality control and uncertainty analysis of Round - trip](#)  
741 [drifting sounding system data, \*Chinese J. Atmos. Sci.\*, 44, 20, \[9895.1912.19203, 2020. \\(in Chinese\\)\]\(https://doi.org/10.3878/j.issn.1006 -</a></a><br/>742 <a href=\)](#)

743 [Wang, R. W., Han, W., Tian, W. H., Gong, J. D.: Blacklist Design of AMDAR Temperature Data and Their](#)  
744 [Application in the CMA-GFS, \*J. Trop. Meteorol.\*, 27, 368–377, \[8775.2021.032, 2021.\]\(https://doi.org/10.46267/j.1006-</a></a><br/>745 <a href=\)](#)

746 [Wang, F., Gong, J. D., Wang, R. C., Chen, Y. D.: A methodological study of the CMA global hybrid four-](#)  
747 [dimensional variational data assimilation system, \*Acta Meteorol. Sin.\*, 82\(5\), 709–](#)  
748 [720, <https://qxxb.cmsjournal.net/cn/article/doi/10.11676/qxxb2024.20230140>, 2024. \(in Chinese\)](#)

749 [Wang, R. W., Wang, J. C., Wang, D., Tao, Y. W., Tian, W. H.: Study on the Influence of Return Sounding](#)  
750 [Observation System Based on CMA-MESO, \*Meteorol. Mon.\*, 49\(1\), 52–](#)  
751 [61, <https://doi.org/10.7519/j.issn.1000-0526.2022.032601>, 2023. \(in Chinese\)](#)

752 [Wang, J. C., Wang, D., Wang, R. W., Tan, J., Rong, N.: Assimilation of Round-Trip Horizontal Drift](#)  
753 [Radiosonde Data in CMA-MESO 3DVar and Its Impact on Model Forecast, \*Meteorol. Mon.\*, 50\(2\), 50–](#)  
754 [60, <https://doi.org/10.7519/j.issn.1000-0526.2023.110501>, 2024. \(in Chinese\)](#)

755 [Wang, J. C., Wang, D., Yang, R. K., Cao, X. Z., Guo, Q. Y.: A Return Radiosonde Trajectory Forecast Method](#)  
756 [and Its Preliminary Evaluation Based on High Resolution Numerical Weather Prediction Model, \*Chinese J.\*](#)  
757 [Atmos. Sci., 45, 651–663, <https://doi.org/10.3878/j.issn.1006 - 9895.2012.20186>, 2021.](#)

758 [Wen, Q. S., Zhang, X. F., Hu, S., Zhao, P. T., Zhong, S. X., Liu, Z. Y., Zhao, Z. K., Liang, J. H., Dai, G. F.,](#)  
759 [Zhang, C. Z., Li, M. J., Huang, L.: Collaborative assimilation experiment of Beidou radiosonde and drone-](#)  
760 [dropped radiosonde based on CMA-TRAMS, \*Atmos. Oceanic Sci. Lett.\*,](#)  
761 [18\(2\), <https://doi.org/10.1016/j.aosl.2024.100555>, 2025.](#)

762 [Wang, J. H., Young, K., Hock, T., Lauritsen, D., Behringer, D., Black, M., Black, P. G., Franklin, J., Halverson,](#)  
763 [J., Molinari, J., Nguyen, L., Reale, T., Smith, J., Sun, B., Wang, Q., Zhang, J. A.: A long-term, high-quality,](#)  
764 [high-vertical resolution GPS dropsonde data set for hurricane and other studies, \*Bull. Am. Meteorol. Soc.\*,](#)  
765 [96, 961-973, <https://doi.org/10.1175/BAMS-D-13-00203.1>, 2015.](#)

766 WMO (World Meteorological Organization): 8th WMO Workshop on the Impact of Various Observing Systems  
767 on Numerical Weather Prediction and Earth System Prediction, Norrköping, Sweden,  
768 <https://community.wmo.int/en/meetings/8th-wmo-impact-workshop-home>, 2024.

769 WMO (World Meteorological Organization): Guide to Meteorological Instruments and Methods of Observation,  
770 Volume III - Observing Systems, WMO-No. 8, Page 464, pp., <https://library.wmo.int/idurl/4/41650>, 2025  
771 edition.

772 WMO (World Meteorological Organization): Instruments and Observing Methods Report No. 143: Report of  
773 WMO's 2022 Upper-Air Instruments Intercomparison Campaign, Geneva, 22  
774 pp., <https://library.wmo.int/idurl/4/68808>, 2024.

775 WMO (World Meteorological Organization): The gaps in the Global Basic Observing Network (GBON), SOFF  
776 Series No. 2, Page 4, pp., <https://library.wmo.int/idurl/4/57174>, 2020.

删除[CMA MOC luo]: 2022,

删除[CMA MOC luo]: doi:

删除[CMA MOC luo]: 27 - 30 May 2024

删除[CMA MOC luo]: ,

删除[CMA MOC luo]: doi:

删除[CMA MOC luo]: Wang, J. H., Young, K., Hock, T.,  
Lauritsen, D., Behringer, D., Black, M., Black, P. G., Franklin,  
J., Halverson, J., Molinari, J., Nguyen, L., Reale, T., Smith, J.,  
Sun, B., Wang, Q., Zhang, J. A.: A long-term, high-quality,  
high-vertical resolution GPS dropsonde data set for hurricane

删除[CMA MOC luo]: 2025 edition

删除[CMA MOC luo]: ,

删除[CMA MOC luo]: doi:

删除[CMA MOC luo]: 2024,

删除[CMA MOC luo]: doi:

删除[CMA MOC luo]: 2020,

删除[CMA MOC luo]: doi:

删除[CMA MOC luo]:

删除[CMA MOC luo]: Wang, D., Wang, J. C., Tian, W. H.,  
Guo, Q. Y.: Quality control and uncertainty analysis of Round  
- trip drifting sounding system data, *Chinese J. Atmos. Sci.*,  
2020, 44, 20, doi:<https://doi.org/10.3878/j.issn.1006 ->  
9895.1912.19203. (in Chinese)

777 Xu, H. F., Guo, Q. Y., Liu, Y. Z., Lin, T. N., Ma, P. Q., and Dong, F. Z.: Key factors influencing drift success  
778 rate of new-type meteorological balloons, *Journal of Applied Meteorological Science.*, 36(4), 427-440,  
779 <https://doi.org/10.11898/1001-7313.20250404>, 2025. (in Chinese)

780 Yang, R. K., Wang, Y., and Liu, Q. Q.: Dynamic Performance Analysis of Sounding temperature sensor, *Sci.*  
781 *Technol. Eng.*, 4 (57-60), <https://doi.org/10.3969/j.issn.1671-1815.2014.04.012>, 2014. (in Chinese)

782 Yang, J. C., Wang, Y. M., Li Q. J., Jia K. B., and Liu, P. Y.: Research on error prediction technology of  
783 radiosonde temperature sensor, *Journal of Electronic Measurement and Instrumentation.*, 35(12):24-26,  
784 <https://doi.org/10.13382/j.jemi.B2104288>, 2022. (in Chinese)

785 Yao, L.B., Shen, D., Sun, X., Wang, D.H., Cao, X.Z., Wang, J.C., Wang, D., Zhang, C.Y., Guo, Q.Y.: Ascent-  
786 drift-descent radiosonde system: Field experiments and data quality assessment, *Atmospheric Research.*,  
787 329, 108489, <https://doi.org/10.1016/j.atmosres.2025.108489>, 2026.

788 Yang, C. Y., Guo, Q.Y., Cao, X.Z., Zhang, W.: Analysis of gravity wave characteristics in the lower  
789 stratosphere based on new round-trip radiosonde, *Acta Meteorologica Sinica.*, 79(1):150-167,  
790 <https://doi.org/10.11676/qxxb2021.008>, 2021. (in Chinese)

791 Yang, C. Y., Cao, X.Z., Guo, Q.Y., Yuan, Y.: Feature Extraction and Analysis of Atmospheric Turbulence  
792 Based on New Round-Trip Radiosonde, *Chinese Journal of Atmospheric Sciences.*, 47(6): 1967–1982,  
793 <https://www.iapjournals.ac.cn/dqkx/article/exportPdf?id=bbe5bcd7-643c-4986-b364-2260622abbda>, 2023.  
794 (in Chinese)

795 Zhang, X. P., Guo, Q. Y., Yang, R. K., Ma, X. L., Cao, X. Z.: Assimilation Experiment of Rainstorm in the  
796 Middle and Lower Reaches of the Yangtze River Based on "ascent-drift-descent" Sounding Data, *Meteorol.*  
797 *Mon.*, 47(12), 1512–1524, <https://doi.org/10.7519/j.issn.1000-0526.2021.12.007>, 2021. (in Chinese)

798 Zhang, C. Z., Huang, Y. Y., Liang, J. H., Xu, H. F.: Application Experiment of Assimilating Beidou Satellite  
799 Navigation Round-Trip Sounding Data Observed in Guangdong Province Using CMA-GD Model, *Journal*  
800 *of Tropical Meteorology.*, 41(1) ,16-25, <https://doi.org/10.16032/j.issn.1004-4965.2025.001>, 2025. (in  
801 Chinese)

802 Zhang, X., Wang, Q. P., Ma, X. L., Zhang, X. P., Cheng, W., Xia, Y. C.: The Influence of New Round-Trip  
803 Drifting Sounding Observation on the Quality of Numerical Prediction in the Middle and Lower Reaches  
804 of the Yangtze River, *Chinese Journal of Atmospheric Sciences.*, 49(1): 245–256,  
805 <https://doi.org/10.3878/j.issn.1006-9895.2304.22224>, 2025. (in Chinese)

806 Zhang, X. P., Sun, L., Ma, X. L., Guo, H., Gong, Z. R., Yan, X. H.: Can the Assimilation of the Ascending and  
807 Descending Sections' Data from Round-Trip Drifting Soundings Improve the Forecasting of Rainstorms in  
808 Eastern China?, *Atmosphere.*, 14, 1127, <https://doi.org/10.3390/atmos14071127>, 2023.

809 Zhang, X. F., Li, L. X., Yang, R. K., Guo, R., Sun, X., Luo, J. P., Chen, H. B., Liu, D. X., Tang, K. B., Peng, W.  
810 W., Han, X. D., Guo, Q. Y., Li, X. X., Fei, X. K.: Comprehensive Marine Observing Experiment Based on  
811 High-Altitude Large Unmanned Aerial Vehicle (South China Sea Experiment 2020 of the "Petrel  
812 Project"), *Adv. Atmos. Sci.*, 38, 531–537, <https://doi.org/10.1007/s00376-020-0314-1>, 2021.

813 Zhou, X. S., Guo Q.Y., Xia Y.C., Tian, H.: Inspection of FY-3D satellite temperature data based on horizontal  
814 drift round-trip sounding data, *J Appl Meteor Sci.*, 34(1): 52-64, [10.11898/1001-7313.20230105](https://doi.org/10.11898/1001-7313.20230105), 2023. (in  
815 Chinese)

删除[CMA MOC luo]: et al  
删除[CMA MOC luo]: 2025,  
删除[CMA MOC luo]: .  
删除[CMA MOC luo]: doi:  
删除[CMA MOC luo]: 2014,  
删除[CMA MOC luo]: doi:  
删除[CMA MOC luo]: et al  
删除[CMA MOC luo]: 2022,  
删除[CMA MOC luo]: .  
删除[CMA MOC luo]: doi:  
设置格式[CMA MOC luo]: 字体颜色: 自动设置  
删除[CMA MOC luo]: ., 2026  
设置格式[CMA MOC luo]: 字体颜色: 自动设置  
删除[CMA MOC luo]: .  
设置格式[CMA MOC luo]: 字体颜色: 自动设置  
设置格式[CMA MOC luo]: 字体颜色: 自动设置  
删除[CMA MOC luo]: .  
设置格式[CMA MOC luo]: 字体颜色: 自动设置  
设置格式[CMA MOC luo]: 字体颜色: 自动设置, 非删除线  
删除[CMA MOC luo]: .  
删除[CMA MOC luo]: 2021,  
删除[CMA MOC luo]: .  
删除[CMA MOC luo]: doi:  
删除[CMA MOC luo]: et al  
删除[CMA MOC luo]:  
删除[CMA MOC luo]: [J].  
删除[CMA MOC luo]: (in Chinese), 2023,  
删除[CMA MOC luo]: .  
删除[CMA MOC luo]: doi:https://  
删除[CMA MOC luo]: Zhu, H. J., Li, F. Z., Kan, Z. P., H  
删除[CMA MOC luo]: -  
删除[CMA MOC luo]: -  
删除[CMA MOC luo]: 2021,  
删除[CMA MOC luo]: doi:

816	Zhou, X. S., Hong G., Xia Y.C., Luo H.W., Bao W.Z., Tian H.: <a href="#">Verification of FY-3D Satellite Humidity Profiles Using Descending Phase Data of Round-Trip Drifting Sounding</a> , <i>Meteor Mon.</i> , <b>50</b> (11): 1373-1385,	删除[CMA MOC luo]: ,
817		删除[CMA MOC luo]: [J].
818	<a href="http://dx.doi.org/10.7519/j.issn.1000-0526.2024.063002">http://dx.doi.org/10.7519/j.issn.1000-0526.2024.063002</a> , 2024. (in Chinese)	删除[CMA MOC luo]: 2024,
819	<a href="#">Zhu, H. J., Li, F. Z., Kan, Z. P., He, H., Xiao, D. E., Zhang, L. Q.: Latex balloons buoyancy change analysis and vertical motion trajectory simulation</a> , <i>J. Rubber Ind.</i> , <b>68</b> (8), <a href="https://doi.org/10.12136/j.issn.1000-890-x.2021.01.0017">https://doi.org/10.12136/j.issn.1000-890-x.2021.01.0017</a> , 2021. (in Chinese)	设置格式[CMA MOC luo]: 字体颜色: 自动设置
820		删除[CMA MOC luo]: Zhang, C. Z ., et al.: Application
822	Zhuang, Z. R., Wang, R. C., Wang, J. C., Gong, J. D.: GRAPES_Meso background error characteristics and application, <i>J. Appl. Meteorol. Sci.</i> , <b>30</b> (3), 316–331, <a href="https://doi.org/10.11898/1001-7313.20190306">https://doi.org/10.11898/1001-7313.20190306</a> , 2019.	Experiment of Assimilating Beidou Satellite Navigation Round-Trip Sounding Data Observed in Guangdong Province Using CMA-GD Model, <i>Journal of Tropical Meteorology</i> , 2025, 41(1) ,16-25,doi: <a href="https://doi.org/10.16032/j.issn.1004-4965.2025.001">https://doi.org/10.16032/j.issn.1004-4965.2025.001</a> .(in Chinese)
823		Zhang, X, Wang Q. P, MA, X.L, et al. .: The Influence of New Round-Trip Drifting Sounding Observation on the Quality of Numerical Prediction in the Middle and Lower Reaches of the Yangtze River [J]. <i>Chinese Journal of Atmospheric Sciences</i> , 2025, 49(1): 245–256. doi: <a href="https://doi.org/10.3878/j.issn.1006-9895.2304.22224">https://doi.org/10.3878/j.issn.1006-9895.2304.22224</a> .(in Chinese)
824	(in Chinese)	Zhang, X. P., Sun, L., Ma, X. L., et al.: Can the Assimilation of the Ascending and Descending Sections' Data from Round-Trip Drifting Soundings Improve the Forecasting of Rainstorms in Eastern China? <i>Atmosphere.</i> , 2023, 14, 1127. doi: <a href="https://doi.org/10.3390/atmos14071127">https://doi.org/10.3390/atmos14071127</a> .
825	▼	删除[CMA MOC luo]: 2019,
		删除[CMA MOC luo]: doi:
		删除[CMA MOC luo]: Zhang, X. F., Li, L. X., Yang, R. K., et al.: Comprehensive Marine Observing Experiment Based on High-Altitude Large Unmanned Aerial Vehicle (South China Sea Experiment 2020 of the “Petrel Project”). <i>Adv. Atmos. Sci.</i> 38, 531–537 (2021). doi: <a href="https://doi.org/10.1007/s00376-020-0314-1">https://doi.org/10.1007/s00376-020-0314-1</a> .